

# Aluminum 26 production in asymptotic giant branch stars

N. Mowlavi<sup>1,2</sup> and G. Meynet<sup>1</sup>

<sup>1</sup> Geneva Observatory, 1290 Sauverny, Switzerland

<sup>2</sup> INTEGRAL Science Data Center, Switzerland

Received 16 March 2000 / Accepted 27 June 2000

**Abstract.** The production of <sup>26</sup>Al in asymptotic giant branch (AGB) stars is studied based on evolutionary stellar models of different masses ( $1.5 \leq M/M_{\odot} \leq 6$ ) and metallicities ( $0.004 \leq Z \leq 0.02$ ). It is confirmed that <sup>26</sup>Al is efficiently produced by hydrogen burning, but destruction of that nuclei by n-capture reactions during the interpulse and pulse phases becomes increasingly more efficient as the star evolves on the AGB.

The amount of <sup>26</sup>Al available in the intershell region follows, at a given metallicity, a very well defined pattern as a function of the H-burning shell temperature  $T_H$ . Two zones must be distinguished. The first one comprises those He-rich layers containing H-burning ashes which escape pulse injection. The amount of <sup>26</sup>Al in that zone ( $1-2 \times 10^{-7} M_{\odot}$  at the first pulse in  $1.5-3 M_{\odot}$   $Z=0.02$  stars) steadily decreases with pulse number. Its contribution to the surface <sup>26</sup>Al enhancement can only be important during the first pulses if dredge-up occurs at that stage. The second zone consists of the C-rich material emerging from the pulses. The amount of <sup>26</sup>Al available in that zone is higher than that in the first zone ( $3-4 \times 10^{-7} M_{\odot}$  at the first pulse in  $1.5-3 M_{\odot}$   $Z=0.02$  stars), and keeps constant during about the first dozen pulses before decreasing when  $T_H \gtrsim 55 \times 10^6$  K. This zone is thus an important potential reservoir for surface <sup>26</sup>Al enrichment.

Using third dredge-up (3DUP) efficiencies from model calculations, the surface <sup>26</sup>Al abundance is predicted to reach  $1-2 \times 10^{-7}$  mass fractions in our low-mass solar metallicity stars, with an uncertainty factor of about three. It decreases with increasing stellar mass, being about three times lower in a  $4 M_{\odot}$  than in  $2-3 M_{\odot}$  stars. In massive AGB stars, however, hot bottom burning enables to easily reach surface <sup>26</sup>Al mass fractions above  $10^{-6}$ .

The <sup>26</sup>Al/<sup>27</sup>Al ratios measured in meteoritic SiC and oxide grains are discussed, as well as that possibly measured in the nearby C-star IRC+10216. We also address the contribution of AGB stars to the  $2-3 M_{\odot}$  present day mass of <sup>26</sup>Al detected in the Galaxy.

Finally, we discuss the possibility of directly detecting an AGB star or a planetary nebula as a single source at 1.8 MeV with the future INTEGRAL satellite.

**Key words:** stars: abundances – stars: interiors – stars: evolution – stars: white dwarfs – stars: carbon – stars: AGB and post-AGB

---

## 1. Introduction

<sup>26</sup>Al is an interesting radioactive nuclei in many respects. With a mean decay lifetime of  $\tau = 1.053$  million years, it is at the origin of the 1.8 MeV diffuse Galactic emission first observed by the HEAO 3  $\gamma$ -ray spectroscopy experiment (Mahoney et al. 1984) and confirmed by many subsequent observations. The Compton Gamma Ray Observatory (CGRO) Comptel 1.8 MeV sky map (Oberlack et al. 1996) suggests the presence of  $2-3 M_{\odot}$  of <sup>26</sup>Al in our Galaxy today (Knödseder 1999), while the measurements by the Gamma-Ray Imaging Spectrometer (GRIS) might be compatible with higher values up to  $\sim 5 M_{\odot}$  (Naya et al. 1998). These last authors suggest that a significant fraction of the <sup>26</sup>Al emission may come from extended sources with low surface brightness that are invisible to COMPTEL.

<sup>26</sup>Al is also made responsible for the <sup>26</sup>Mg overabundances measured in meteoritic material. Indeed <sup>26</sup>Al belong to the set of short-lived radioactive elements believed to have decayed in situ in meteorites (see the review by Podosek & Nichols 1997). The canonical value of the <sup>26</sup>Al/<sup>27</sup>Al ratio amounts to  $5 \times 10^{-5}$  (Lee et al. 1977; MacPherson et al. 1995) and corresponds to its mean value in the bulk of the solar system material at the time of its formation 4.57 billion years ago. Ratios 2 to 5 orders of magnitudes greater than the canonical value have been measured in some meteoritic grains (e.g. Hoppe & Ott 1997, Nittler 1997), generally accompanied by non solar ratios of other isotopic ratios (such as <sup>13</sup>C/<sup>12</sup>C, <sup>15</sup>N/<sup>14</sup>N and <sup>18</sup>O/<sup>16</sup>O). These meteoritic grains are considered nowadays as pristine circumstellar grains having survived the process of solar system formation. As such, they carry important nucleosynthesis information on the parent star around which the grain initially formed.

Several stellar sites are proposed in the literature for the synthesis of <sup>26</sup>Al. Supernovae have been suggested by Arnett & Wefel (1978), novae by Vangioni-Flam et al. (1980), asymptotic giant branch (AGB) stars by Norgaard (1980) and Wolf-Rayet stars by Dearborn & Blake (1985). Among the most recent works giving <sup>26</sup>Al abundance predictions for these sources, we mention Timmes et al. (1995) for type II supernovae, Jordi et

al. (1997) and Kolb & Politano (1997) for novae, Forestini & Charbonnel (1997) for AGB stars, and Meynet et al. (1997) for Wolf–Rayet stars. New sources of  $^{26}\text{Al}$  have also been studied recently. Clayton (1994) suggests that  $^{26}\text{Al}$  could be produced by low energy heavy cosmic rays in molecular clouds, while Langer et al. (1998) analyses the contribution from massive close binaries.

Stellar model calculations including an adequate nucleosynthesis network could, in principle, ascertain the relative contribution of each of the stellar sites to the Galactic  $^{26}\text{Al}$  production and provide isotopic ratio predictions. Unfortunately, available  $^{26}\text{Al}$  yields are subject to uncertainties affecting both nuclear reaction rates and stellar model calculations. A comparison of the spatial distribution of the Galactic 1.8 MeV emission as derived by CGRO COMPTEL with those at other wavelengths suggests a preponderant contribution of massive stars to the Galactic  $^{26}\text{Al}$  production (Knödseder et al. 1999). However, as mentioned above, the GRIS data may suggest a non negligible contribution from extended sources with low surface brightness such as AGB stars. The fact that AGB stars do indeed produce  $^{26}\text{Al}$  is strongly supported by the high  $^{26}\text{Al}/^{27}\text{Al}$  ratios measured in silicon carbide (SiC) grains, knowing that those grains are found around the majority of AGB stars (as attested by their 11.3 micron absorption or emission feature, see Cherchneff & Cau 1999 for a review). The possible observation of  $^{26}\text{Al}$  itself in the outer envelope of a nearby carbon star (Guélin et al. 1995) would be, if confirmed, a direct evidence for the production of that element in those stars.

In this work we reevaluate the production of  $^{26}\text{Al}$  by AGB stars, with particular attention to the uncertainties affecting its yields. The dredge–up of  $^{26}\text{Al}$  from the deep stellar layers where it is produced to the surface is also treated more consistently in the light of the latest model predictions. The physical ingredients of our AGB models are presented in Sect. 2, while the production mechanism of  $^{26}\text{Al}$  in those stars is reviewed in Sect. 3. Sect. 4 presents our model predictions concerning  $^{26}\text{Al}$ , and Sect. 5 analyses the mass of that element ejected by AGB stars. Comparison of those predictions to observational data is presented in Sect. 6. Conclusions are drawn in Sect. 7.

## 2. The models

Seven stellar models are computed from the pre–main sequence up to the AGB phase, with initial masses  $M$  and metallicities  $Z$  (the metallicity refers to the mass fraction of all elements heavier than helium)  $(M/M_{\odot}, Z) = (1.5, 0.018), (2.5, 0.018), (3, 0.020), (4, 0.018), (6, 0.020), (2.5, 0.008)$  and  $(2.5, 0.004)$ . About 6000 models are calculated prior to the AGB phase for the intermediate–mass ( $M \gtrsim 2 M_{\odot}$ ) stars. The calculation of the  $1.5 M_{\odot}$  star requires more models because it develops a degenerate core after core H exhaustion. The subsequent evolution of that star is characterized by a long giant branch phase of about  $2 \times 10^9$  y during which H burns in a shell. Helium eventually ignites in the degenerate core, which leads to a thermal runaway called He–flash. The degeneracy is waived by the expansion of the central regions and the star resumes core He–

**Table 1.** Solar abundances, in mass fraction, of the stable nuclei involved in the Mg–Al chain of H–burning. The solar metallicity is taken equal to  $Z = 0.018$ .

nuclei	solar mass fraction
$^{23}\text{Na}$	$3.17 \times 10^{-5}$
$^{24}\text{Mg}$	$4.89 \times 10^{-4}$
$^{25}\text{Mg}$	$6.42 \times 10^{-5}$
$^{26}\text{Mg}$	$7.37 \times 10^{-5}$
$^{27}\text{Al}$	$5.50 \times 10^{-5}$
$^{28}\text{Si}$	$6.20 \times 10^{-4}$

burning until it reaches the AGB phase. The red giant branch and He–flash phase of the  $1.5 M_{\odot}$  star are consistently followed in about 12 000 and 1 000 models, respectively.

The models presented in this paper are the same as those analyzed in Mowlavi (1999b, hereafter denoted by M99) for sodium production during the AGB phase. Several of the model specifications can be found in that paper and are not repeated here. We only present some additional features of relevance for the study of  $^{26}\text{Al}$ .

The abundance profiles of 47 nuclei from H to S are followed consistently with the stellar structure all along the evolution. The ground state  $^{26}\text{Al}^g$  and the isomeric state  $^{26}\text{Al}^i$  of  $^{26}\text{Al}$  are considered as two distinct species in the Mg–Al chain of H–burning. The initial abundances are taken from Anders & Grevesse (1989) scaled to the required metallicity. Those involved in the synthesis of  $^{26}\text{Al}$  are listed in Table 1 for solar composition. The appendix summarizes the main features of the Mg–Al chain and gives the relevant nuclear reaction rates used in the models. The impact of the new NACRE reaction rates on the Mg–Al chain is also discussed in that Appendix.

Mass loss is taken into account from the red giant branch on according to the Reimers formula

$$\dot{M} = -\eta \times 4 \cdot 10^{-13} \times \frac{L R}{M}, \quad (1)$$

$L$ ,  $R$  and  $M$  being the actual stellar luminosity, radius and mass, respectively, in solar units. The parameter  $\eta$  is taken equal to 0.33 during the red giant branch phase (relevant only for the  $1.5 M_{\odot}$  star), and equal to one during the AGB phase. The implications of a superwind scenario terminating abruptly the AGB phase are analyzed in Sect. 6.

The treatment of mixing represents a main issue for the prediction of surface abundances. Convective mixing in AGB stars is made responsible for the transport of the ashes of both H– and He–burning from the deep layers where they are synthesized to the surface (process called ‘third dredge–up’, denoted hereafter 3DUP). As in most AGB models available in the literature, we use the mixing length theory for convection (with a mixing length to pressure scale height ratio of  $\alpha_{mlt} = 1.5$ ), and the Schwarzschild criterion for the determination of the boundaries of convective zones. Such a local criterion, however, is known to lead to the development of an unphysical discontinuity in the chemical abundance profiles when the H–rich envelope penetrates into the H–depleted layers, and prevents the

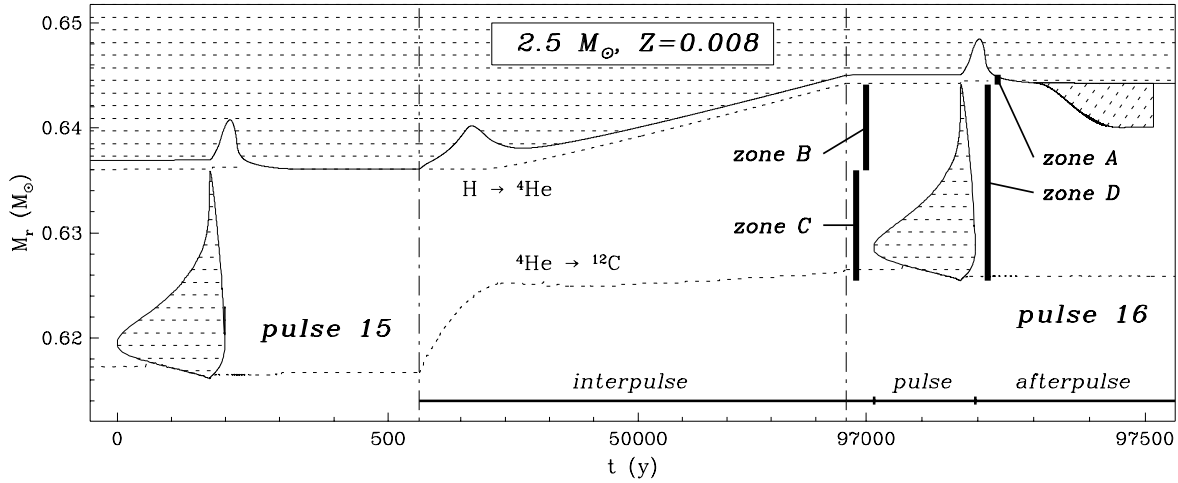


**Fig. 1.** Structural evolution of the intershell regions of the  $2.5 M_{\odot}$  model star with  $Z = 0.008$  between the 15th and 16th pulse. The origin of the abscissa is arbitrarily set to the time of onset of pulse 15. Filled regions correspond to convective zones. The dotted lines identify the location of maximum energy production in the H-burning (top) and He-burning (bottom) layers. The different phases of an instability cycle and zones A–D of the intershell layers described in Sect. 3.1 of the main text are also indicated. The simulation of a third dredge-up is shown in the afterpulse phase of pulse 16 (region hatched at 45 degrees in the rightmost subpanel). Note that the time abscissa has different scales in each of the panels displaying pulse 15, the interpulse and pulse 16.

adequate operation of 3DUP (Mowlavi 1999a). Those standard<sup>1</sup> models are thus inadequate for a consistent prediction of *surface* abundances. The use of some kind of diffusive extra-mixing below the convective envelope can remove the discontinuity and enable a consistent modeling of the 3DUP. Such a procedure, however, is very computer time consuming. For that reason, and in order to analyze the  $^{26}\text{Al}$  production in a variety of AGB models of different masses and metallicities, the seven models presented here are performed without extra-mixing. The surface  $^{26}\text{Al}$  abundances are then computed a posteriori using synthetic AGB calculations (Sect. 5).

### 3. $^{26}\text{Al}$ production in AGB stars

#### 3.1. AGB stars

A recent review on the structural and chemical evolution of AGB stars can be found in, among many others, Busso et al. (1999). Briefly, those objects are characterized by two burning shells, one of helium (noted HeBS) of about  $10^{-2} M_{\odot}$  and one of hydrogen (HBS) of some  $10^{-4} M_{\odot}$ , and by a deep convective envelope extending from above the HBS up to the surface. The HeBS is thermally unstable and periodically liberates  $10^2$  to  $10^6$  times the energy provided by the H-burning shell. Those outbursts lead to the development of a convective tongue (called ‘pulse’) in the HeBS. As in M99, we divide an instability cycle into three phases, the interpulse, the pulse and the after pulse phase (illustrated in Fig. 1).

<sup>1</sup> Standard models refer, in this paper, to models using the Schwarzschild criterion to delimit convective zones without applying any extra-mixing procedure such as overshooting or diffusive mixing induced by rotation.

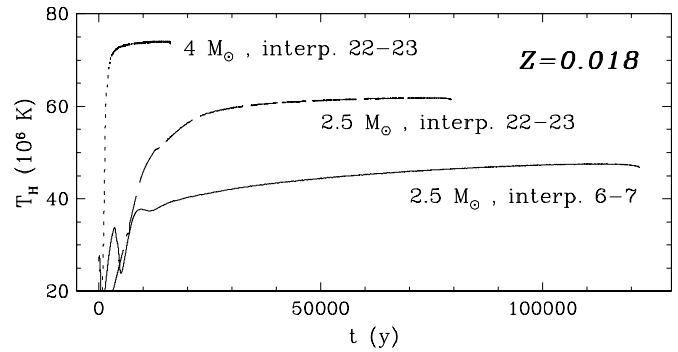


**Fig. 2.** Evolution of the temperature of the hydrogen burning shell at the layer of maximum energy production during the 6th (solid line) and 22nd (dashed line) interulses of the  $2.5 M_{\odot}$ ,  $Z = 0.018$  model star, and during the 22nd interpulse of the  $4 M_{\odot}$  star of the same metallicity.

*Interpulse phase:* During the interpulse phase, hydrogen burns in a thin layer located at mass fractions  $M_r$  increasing with time. The HeBS is almost extinct. This phase lasts  $10^4$  to  $10^5$  years, depending on the stellar mass, metallicity and interpulse number. The more massive or less metal-rich the star, the shorter the interpulse duration.

The temperature of the HBS keeps an almost constant value during a given interpulse (after a fast rise at the beginning of that phase, see Fig. 2). Its value  $T_H$  at the end of each interpulse phase is given in Fig. 3 for all our model stars. It is seen to readily increase from one interpulse to the next, starting with values higher than  $40 \times 10^6$  K in all our stars. In the  $3 M_{\odot}$  star (filled squares in Fig. 3), for example,  $T_H$  increases from  $43 \times 10^6$  K at the first pulse to above  $63 \times 10^6$  K at the 20th interpulse, while  $T_H$  reaches values above  $70 \times 10^6$  K in the 4 and  $6 M_{\odot}$  stars. In general,  $T_H$  is higher in stars with higher masses or lower

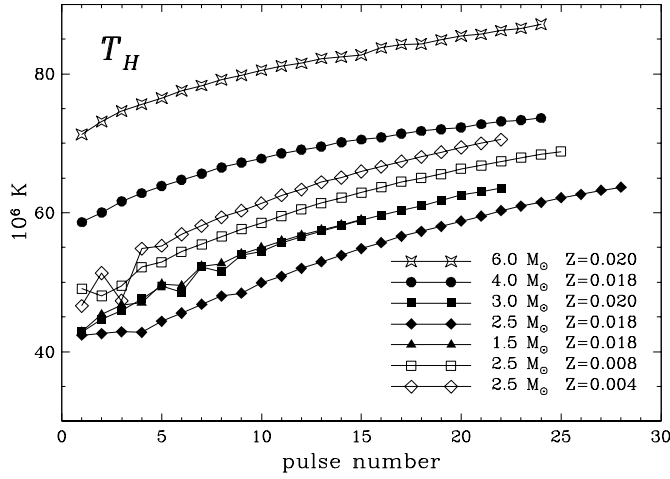


**Fig. 3.** Temperature, as a function of pulse number, of the hydrogen burning shell at the layer of maximum energy production and at the onset of each pulse in all the model stars as labeled in the graph.

metallicities. The  $1.5 M_{\odot}$  model star is an exception with HBS temperatures higher than in the  $2.5 M_{\odot}$  star (at similar metallicities) and comparable to the ones in the  $3 M_{\odot}$  model star. This peculiarity is due to the fact that the  $1.5 M_{\odot}$  star experiences a long red giant branch phase after the main sequence, during which the H-depleted core mass already increases significantly.

From a chemical point of view, the ashes left over by the HBS mainly consist of  $^{14}\text{N}$ , the main product emerging from the CNO cycle. Of importance to our study are the  $^{26}\text{Al}$  produced by the Mg–Al chain and the few amounts (to the level of about  $10^{-4}$  mass fractions) of  $^{13}\text{C}$  left over by the CNO cycle. These H-burning ashes accumulate in the underlying He-rich zone. Part of those ashes (those lying in zone A shown in Fig. 1) is directly mixed to the surface by the 3DUP process, but the majority (those in zone B in Fig. 1) is mixed down to higher temperatures during the pulse phase.

*Pulse phase:* As the mass of the He-rich layers increases, a thermal instability is triggered in the HeBS and a convective pulse develops. The convective zone starts at the location of maximum energy production in the HeBS, and extends up close to the HBS (see Fig. 1). It lasts few decades to few centuries, depending on the stellar mass, metallicity, or pulse number. The more massive or less metal-rich the star, the shorter the pulse duration.

The maximum temperature  $T_p$  at the base of a pulse is (almost) reached at the time of maximum pulse extension. Its value in the first pulse depends on the stellar mass and metallicity, but is above  $170 \times 10^6$  K in all our model stars<sup>2</sup> (Fig. 4). It then readily increases pulse after pulse. Like  $T_H$ ,  $T_p$  is higher

<sup>2</sup> The temperature  $T_p$  at the base of the first pulse of our models is slightly lower than in other models found in the literature at similar stellar mass and metallicity. For example,  $T_p = 173 \times 10^6$  K in the first pulse of our  $3 M_{\odot}$  star of solar metallicity, while Boothroyd & Sackmann (1988) obtain about  $186 \times 10^6$  K. This may be due to the different mixing prescriptions used in different codes during the *core*

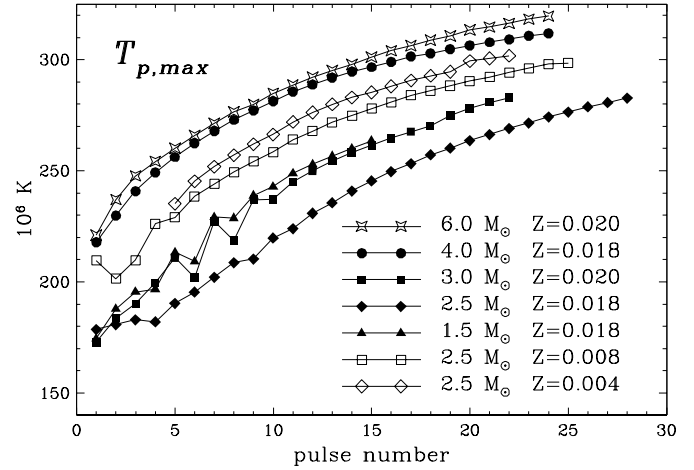


**Fig. 4.** Maximum temperature, as a function of pulse number, at the base of the pulse convective tongues of all the model stars as labeled in the graph.

in stars with higher masses or lower metallicities, the  $1.5 M_{\odot}$  model star making again an exception to this rule as compared to the  $2.5 M_{\odot}$  star of the same metallicity. Actually, there is a univoque and almost linear relation between  $T_H$  and  $T_p$  in AGB stars not experiencing hot bottom burning (i.e. for  $M \lesssim 4 M_{\odot}$  at solar metallicity, see Fig. 5b in M99).

As the pulse grows, it first mixes the C-rich material left over by the preceding pulse in the zone called C in Fig. 1 and then engulfs the ashes of H-burning from zone B.  $^{14}\text{N}$ , in particular, is mixed down to the high temperatures characterizing the pulse, and burns through  $\alpha$ -capture reactions into  $^{18}\text{O}$ . This nuclide, in turn, may burn and synthesize  $^{22}\text{Ne}$  through  $^{18}\text{O}(\alpha, \gamma)^{22}\text{Ne}$ . Those products, among others, are left over by the pulse in zone D.  $^{12}\text{C}$  is of course the main product of He burning through the triple- $\alpha$  reaction. Its intershell mass fraction in zone D amounts to 20–30% in our models (Fig. 4 of M99).

*Afterpulse phase:* During the afterpulse phase, the structural evolution of the intershell layers is dominated by thermal relaxation processes. The temperatures in those intershell layers drop, the H-burning shell extinguishes, and the convective envelope deepens into the H-depleted and, possibly, C-rich layers. The ashes of H-burning which escape the ingestion by the pulse convective tongue (zone A in Fig. 1) and part of the C-rich material from zone D are mixed to the surface. This process is the 3DUP.

The operation of 3DUP in AGB stars is much supported by the peculiar (as compared to other red giants) surface abundances observed at the surface of those stars. Its consistent re-

He-burning phase prior to the AGB phase, in relation to the occurrence of breathing pulses in the convective core. However, the difference is equivalent to the temperature increase over two successive pulses or so, since  $T_p$  reaches 184 and  $190 \times 10^6$  K in the second and third pulses of our  $3 M_{\odot}$  star, respectively. The conclusions reached in this paper concerning the  $^{26}\text{Al}$  production are thus not affected by this slight difference on  $T_p$  with other authors.

production in AGB models, however, was a main problem until recently (Herwig et al. 1997; Mowlavi 1999a). As explained in Sect. 2, our standard models do not self-consistently predict the occurrence of the 3DUP phenomenon. Instead, we use in Sect. 5 dredge-up rules obtained from a separate study of 3DUP in our models.

In summary, four distinct zones are of importance for the analysis of  $^{26}\text{Al}$ . Zone *A* contains HBS ashes which are not engulfed into the pulse and are directly mixed to the surface by the 3DUP. Zones *B* and *C* contain the intershell material which is mixed into the pulse, the former containing H-burning products left over by the HBS and the second C-rich ashes emerging from the previous pulse. This material is processed in the pulse and emerges in zone *D*, a fraction of which (depending on the 3DUP efficiency) is mixed into the envelope by the 3DUP. The masses  $M_A$ ,  $M_B$ ,  $M_C$  and  $M_D = M_B + M_C$  involved in zones *A*, *B*, *C* and *D*, respectively, are functions of the stellar mass, metallicity and pulse number, as shown in Fig. 5 for three of our stellar models.  $M_A$  is of the order of  $10^{-4} - 10^{-3} M_\odot$ , while  $M_B$  and  $M_C$  are about a factor of ten higher. In general, they are smaller in more massive or less metal-rich stars, and decrease with pulse number.

### 3.2. The production and destruction of $^{26}\text{Al}$ in AGB stars

#### 3.2.1. $^{26}\text{Al}$ production

The production of  $^{26}\text{Al}$  in the HBS is governed by the Mg–Al chain of reactions summarized in the Appendix. It is efficiently synthesized at temperatures exceeding  $35 \times 10^6$  K. All AGB stars are thus potential sites for the production of  $^{26}\text{Al}$  in their intershell layers, irrespective of their mass and metallicity (Fig. 3). The first evolutionary AGB models including the Mg–Al chain in the nucleosynthesis network were computed by Forestini et al. (1991) who confirmed the production of  $^{26}\text{Al}$  by those stars.

The main reaction as far as  $^{26}\text{Al}$  production is concerned is  $^{25}\text{Mg}(p, \gamma)^{26}\text{Al}$ . It transforms almost all available  $^{25}\text{Mg}$  into  $^{26}\text{Al}$ . About 80% of the created  $^{26}\text{Al}$  is in the ground state  $^{26}\text{Al}^g$  (half-lifetime of  $7.40 \times 10^5$  yr). The remaining 20% goes into the isomeric state  $^{26}\text{Al}^i$  which disintegrates in 6.3 s into  $^{26}\text{Mg}$ . From an initial  $^{25}\text{Mg}$  mass fraction of  $6.4 \times 10^{-5}$  in solar metallicity stars (Table 1),  $5.3 \times 10^{-5}$  mass fractions of  $^{26}\text{Al}^g$  are thus expected to be formed, while the  $^{26}\text{Mg}$  mass fraction is expected to increase from  $7.4 \times 10^{-5}$  (initial abundance) to  $8.7 \times 10^{-5}$ . This is well verified by model predictions. The abundance profiles at the end of the 6th interpulse in the  $2.5 M_\odot$ ,  $Z=0.018$  star, for example, are displayed in Fig. 6. Given the half-lifetime of  $^{26}\text{Al}^g$  and the 122 000 yr duration of that interpulse, a slight decrease of the intershell  $^{26}\text{Al}^g$  abundance with depth is observed in Fig. 6 together with the concomitant increase in the  $^{26}\text{Mg}$  abundance. The other stable nuclei of the Mg–Al chain are not significantly altered in that star.

When the temperature of the HBS exceeds  $\sim 55 \times 10^6$  K at a more advanced stage on the AGB (or in a more massive or lower metallicity star), several distinctive features appear in the intershell abundance profiles. Those are illustrated in

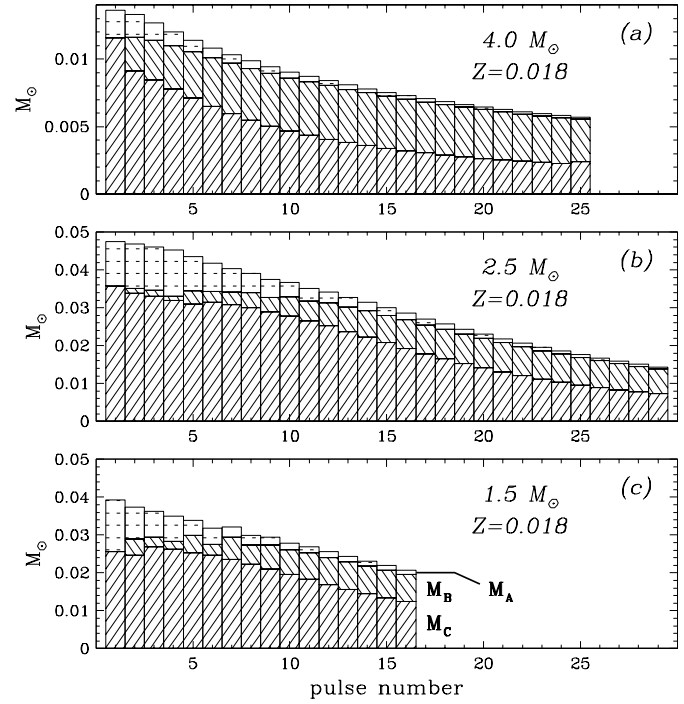


**Fig. 5a–c.** Masses  $M_A$ ,  $M_B$ , and  $M_C$  of each zone *A*, *B* and *C*, respectively, shown in Fig. 1, as a function of pulse number in the 4 (panel a), 2.5 (panel b) and  $1.5 M_\odot$  (panel c) model stars of solar metallicity.  $M_A$ ,  $M_B$  and  $M_C$  are respectively the upper, middle and lower zones of each histogram.

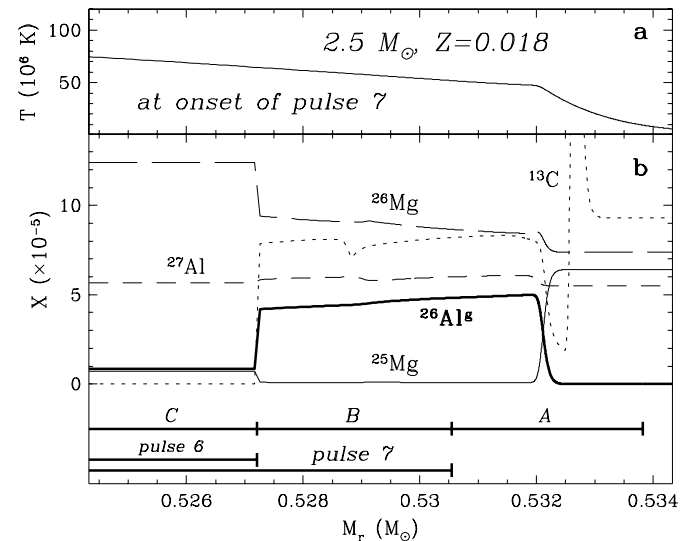


**Fig. 6a and b.** **a** Temperature and **b** abundance profiles of several nuclei, as labeled on the curves, in the intershell layers at the end of the 6th interpulse of the  $2.5 M_\odot$ ,  $Z = 0.018$  model star. The extensions of zones *A*, *B* and *C* described in Sect. 3.1 and of pulses before and after the considered interpulse are also shown in the lower part of panel **b**.

Figs. 7 and 8 which display the intershell abundance profiles at the end of the 22nd interpulse in the  $2.5$  and  $4 M_\odot$  model stars of solar metallicity, respectively. They concern the burning of  $^{24}\text{Mg}$  through  $^{24}\text{Mg}(p, \gamma)^{25}\text{Al}(\beta^+)^{25}\text{Mg}$  and the produc-

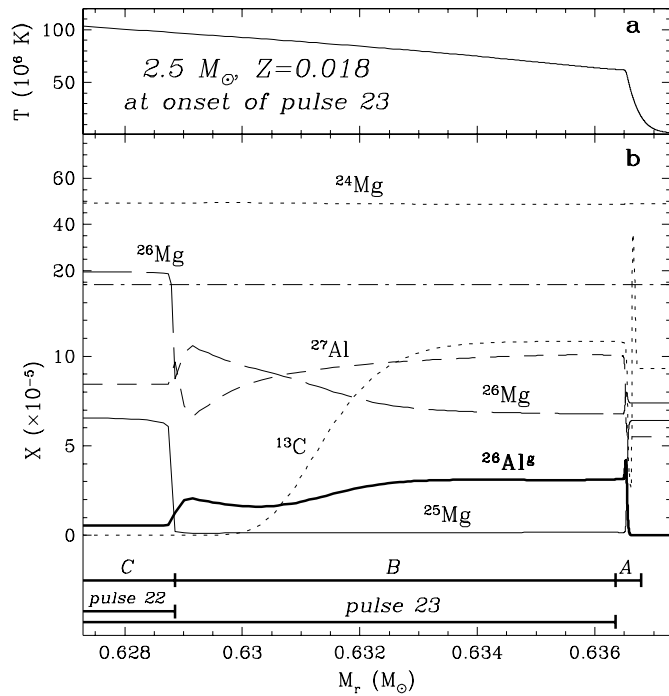


**Fig. 7a and b.** Same as Fig. 6, but at the end of the 22nd interpulse of the  $2.5 M_{\odot}$ ,  $Z = 0.018$  model star. The horizontal dashed–dotted line in panel **b** separates two sub–panels with different tick sizes on the y–abscissa.

tion of  $^{27}\text{Al}$  through  $^{26}\text{Al}^{\text{g}}(p, \gamma)^{27}\text{Si}(\beta^+)^{27}\text{Al}$ . The partial destruction of the abundant  $^{24}\text{Mg}$  nuclei produces  $^{25}\text{Mg}$  and replenishes the Mg–Al chain. Its effect on the  $^{24}\text{Mg}$  abundance profile is clearly visible in the  $4 M_{\odot}$  star (Fig. 8). The  $^{27}\text{Al}$  production, on the other hand, already occurs in the advanced pulses of the  $2.5 M_{\odot}$  star (Fig. 7). Those features reflect the sensitivity of the Mg–Al yields on the temperature at which H–burning occurs (cf. Appendix).

Another distinctive feature of hot interpulses is the intershell  $^{13}\text{C}$  burning by  $\alpha$ –capture during the interpulse phase (Figs. 7 and 8). The resulting  $^{26}\text{Al}$  destruction is addressed below.

### 3.2.2. $^{26}\text{Al}$ destruction

The operation of the Mg–Al chain of H–burning leads to a  $^{26}\text{Al}$  abundance which is roughly independent of temperature above  $35 \times 10^6$  K (see Appendix). This results from the fact that  $^{26}\text{Al}$  destruction through  $^{26}\text{Al}^{\text{g}}(p, \gamma)^{27}\text{Si}(\beta^+)^{27}\text{Al}$  is compensated by the replenishment of the Mg–Al cycle through the partial burning of  $^{24}\text{Mg}$  nuclei as discussed above. The new NACRE reaction rates even predict an increase in the  $^{26}\text{Al}$  yields at temperatures above  $65 \times 10^6$  K (cf. Appendix).  $\beta$ –decay does not lead to significant interpulse  $^{26}\text{Al}$  destruction either, because the interpulse durations are shorter than the decay half–life of that nucleus.

The main source of  $^{26}\text{Al}$  destruction comes from neutron captures through  $^{26}\text{Al}^{\text{g}}(n, p)^{26}\text{Mg}$ . Three neutron sources are

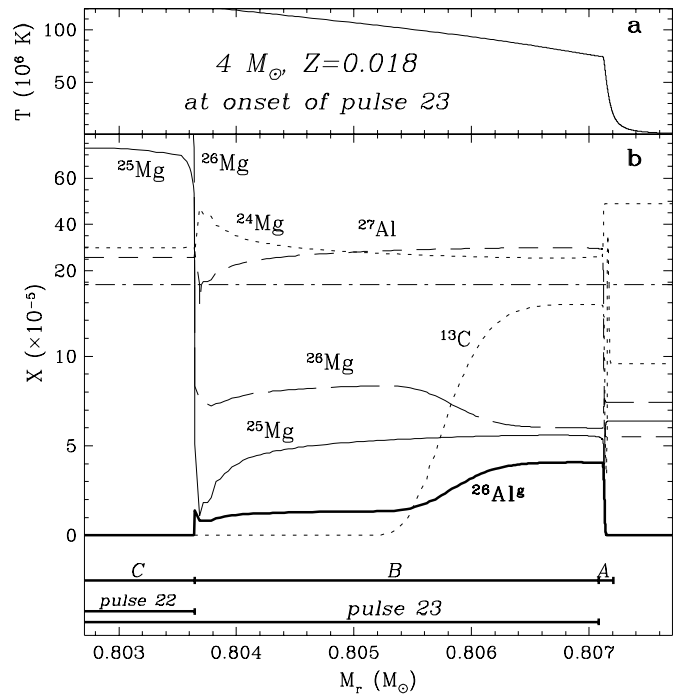


**Fig. 8a and b.** Same as Fig. 6, but at the end of the 22nd interpulse of the  $4 M_{\odot}$ ,  $Z = 0.018$  model star. The horizontal dashed–dotted line in panel **b** separates two sub–panels with different tick sizes on the y–abscissa.

potentially available in AGB stars: secondary  $^{13}\text{C}$ ,  $^{22}\text{Ne}$ , and primary  $^{13}\text{C}$ . These are considered in turn.

**Secondary carbon 13:** Secondary  $^{13}\text{C}$  is left over by the CNO cycles at the level of  $10^{-4}$  mass fractions (Appendix A of M99). When the intershell temperatures reach  $90 \times 10^6$  K, it burns through  $^{13}\text{C}(\alpha, n)^{16}\text{O}$ . The neutrons released by this reaction are partly captured by  $^{26}\text{Al}$ , producing  $^{26}\text{Mg}$  through  $^{26}\text{Al}^{\text{g}}(n, p)^{26}\text{Mg}$ . The  $^{13}\text{C}$  burning and concomitant  $^{26}\text{Al}$  destruction and  $^{26}\text{Mg}$  production are clearly visible in Figs. 7 and 8. In the 22nd interpulse of the  $2.5 M_{\odot}$  star, the  $^{26}\text{Al}$  abundance is reduced by about 30% in the layers where  $^{13}\text{C}$  has burned, while the destruction factor amounts to 60% in the  $4 M_{\odot}$  star at equivalent interpulse number.

The intershell  $^{13}\text{C}$  which remains intact during the interpulse is injected into the next pulse. As it is mixed down to the high pulse base temperatures, it burns through the same reaction channel as during the interpulse, leading to further  $^{26}\text{Al}$  destruction. In the 21st pulse of the  $2.5 M_{\odot}$ ,  $Z = 0.018$  star, for example,  $^{26}\text{Al}$  is further destroyed by 35% due to those neutrons released by  $^{13}\text{C}(\alpha, n)^{16}\text{O}$  in that pulse.

**Neon 22:**  $^{22}\text{Ne}$  becomes a second source of neutrons in pulses when it burns through  $^{22}\text{Ne}(\alpha, n)^{25}\text{Mg}$ . An analysis of  $^{22}\text{Ne}$  burning in our models is already presented in M99 (Sect. 3.4 therein) and is not repeated here. Let us just summarize that  $^{22}\text{Ne}(\alpha, n)^{25}\text{Mg}$  begins to occur at  $T_p$  above  $280 \times 10^6$  K.

Such high temperatures are encountered after a sufficient number of pulses, depending on the stellar mass and metallicity (Fig. 4). The amount of  $^{22}\text{Ne}$  destroyed in the pulses of our model stars remains less than 5% though (except in the 4 and 6  $M_{\odot}$  stars where the  $^{22}\text{Ne}$  destruction factor reaches respectively 10 and 20% in the 24th pulse at  $T_p = 312$  and  $320 \times 10^6$  K, respectively). The amount of neutrons released by  $^{22}\text{Ne}$  burning is nevertheless high enough to lead to a non-negligible destruction of  $^{26}\text{Al}$ . In the 21st pulse of the 2.5  $M_{\odot}$ ,  $Z = 0.018$  star ( $T_p = 265 \times 10^6$  K), for example, where secondary  $^{13}\text{C}$  burning already destroys 35% of the available  $^{26}\text{Al}$ ,  $^{22}\text{Ne}$  is responsible for an additional 15% destruction of that nuclei. The fraction of  $^{26}\text{Al}$  that is destroyed in pulses is actually rather well correlated with pulse temperature, as shown in Sect. 4.

$^{26}\text{Al}$  is thus very fragile with respect to neutron captures and is destroyed with an efficiency which increases with pulse temperature. Yet, as is shown in Sect. 5, the  $^{26}\text{Al}$  abundance emerging in zone *D* is still an important potential reservoir for surface  $^{26}\text{Al}$  replenishment.

*Primary carbon 13:* The existence of a primary source of  $^{13}\text{C}$  in AGB stars is strongly suggested by the observation of fluorine and s-process overabundances (with respect to other red giants) at the surface of many AGB stars (see, respectively, Jorissen et al. 1992 and, e.g., Smith & Lambert 1990). The exact mechanism at the origin of that primary  $^{13}\text{C}$  is still a question of debate. Most probably, some diffusive mixing occurs below the convective envelope during the 3DUP, bringing some protons from that envelope into the C-rich layers. This is suggested by recent models including either diffusive overshooting below the envelope (Herwig et al. 1997) or rotation (Langer et al. 1999).  $^{13}\text{C}$  then forms at H-burning ignition through  $^{12}\text{C}(p, \gamma)^{13}\text{N}(\beta^+)^{13}\text{C}$ . The amount of primary  $^{13}\text{C}$  so formed must be about 10 times higher than the amount of secondary  $^{13}\text{C}$  produced by the HBS in order to match  $^{19}\text{F}$  and s-process abundance observations (Mowlavi et al. 1998). The question of  $^{26}\text{Al}$  destruction then becomes very pertinent.

Model calculations suggest that the primary  $^{13}\text{C}$  burns radiatively during the interpulse phase (Straniero et al. 1995, our own calculations). In that case, only the zone covering the primary  $^{13}\text{C}$  pocket suffers  $^{26}\text{Al}$  destruction during the interpulse. Since the mass extent of that zone, of the order of  $10^{-5}$  to few  $10^{-4} M_{\odot}$ , is very small compared to the  $\sim 0.01 M_{\odot}$  extension of the intershell where  $^{26}\text{Al}$  is present, only a negligible fraction of that  $^{26}\text{Al}$  will be affected by the neutrons released from primary  $^{13}\text{C}$ . We therefore do not worry about the existence of that primary  $^{13}\text{C}$  pocket as far as  $^{26}\text{Al}$  is concerned.

#### 4. Standard model predictions

All the  $^{26}\text{Al}$  production and destruction mechanisms mentioned in Sect. 3.2 are self-consistently taken into account in our evolutionary models (except for the production of primary  $^{13}\text{C}$ , but which should not be of any significant consequence on the  $^{26}\text{Al}$  yields as explained in Sect. 3.2.2). The total masses  $^{26}M_A$ ,  $^{26}M_{B+C}$  and  $^{26}M_D$  of  $^{26}\text{Al}$  predicted by our model stars in

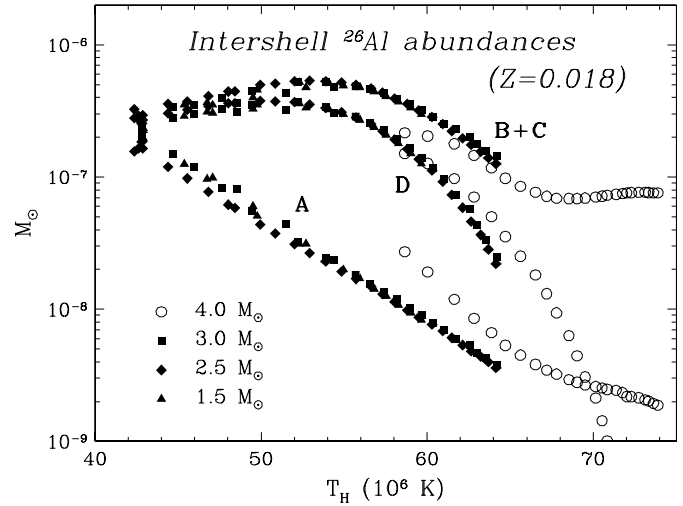


**Fig. 9.** Total masses (in units of solar mass) of  $^{26}\text{Al}$  in zones *A*, *B+C* and *D*, as labeled in the figure, at the time of dredge-ups for our solar metallicity stars. The predictions of the 3  $M_{\odot}$  star have been rescaled from  $Z = 0.020$  to  $Z = 0.018$  for consistency with the other stars. Each mark locates a pulse time.

zones *A*, *B+C* and *D*, respectively, are displayed in Figs. 9 and 10 as a function of the HBS temperature.

$^{26}M_A$  is seen to steadily decrease from one pulse to the next in all the models. In the 3  $M_{\odot}$  star, for example,  $^{26}M_A$  decreases by a factor of 45 from the first to the 20th pulse. This mainly results from the decrease in the mass extent of zone *A* from one pulse to the next. At best (i.e. during the first pulses),  $^{26}M_A = 2 - 3 \times 10^{-7} M_{\odot}$  at solar metallicity. That  $^{26}\text{Al}$  is directly mixed into the envelope during the 3DUPs.

$^{26}M_{B+C}$  first increases slightly as  $^{26}\text{Al}$  builds in the intershell pulse after pulse, then decreases during the hotter interpulses as a result of  $^{13}\text{C}$  burning, and finally reaches a plateau well visible in the 4  $M_{\odot}$  star (Fig. 9). That  $^{26}\text{Al}$  is injected into the next pulse.

The evolution of  $^{26}M_D$  is dictated by  $^{26}\text{Al}$  destruction in the pulses. The percentage of  $^{26}\text{Al}$  burned in the pulses is evaluated from the difference  $^{26}M_{B+C} - ^{26}M_D$  and is shown in Fig. 11. It is very well correlated with the pulse temperature, being small in the first cold pulses ( $\sim 20\%$  destruction at  $200-220 \times 10^6$  K) and increasing with pulse temperature ( $\sim 80\%$  at  $270-285 \times 10^6$  K and close to 100% above  $300 \times 10^6$  K) due to secondary  $^{13}\text{C}$  and  $^{22}\text{Ne}$  burning in the pulses. As a result,  $^{26}M_D$  is close to  $^{26}M_{B+C}$  during the first pulses, and steadily decreases with time at increasing pulse number.

We note the very good correlation between the masses of  $^{26}\text{Al}$  predicted in the intershell zones *A*, *B+C*, *D* and the HBS temperature (Fig. 9). The same holds true at lower metallicities (Fig. 10), but with smaller  $^{26}\text{Al}$  intershell abundances as a result of the smaller initial abundances of  $^{25}\text{Mg}$ .

An important conclusion of our model predictions is the higher masses  $^{26}M_D$  of  $^{26}\text{Al}$  in zone *D*, despite its destruction in the pulses, than in zone *A* during most of the AGB lifetime. Zone *D* is thus a potentially important reservoir for surface  $^{26}\text{Al}$  abun-

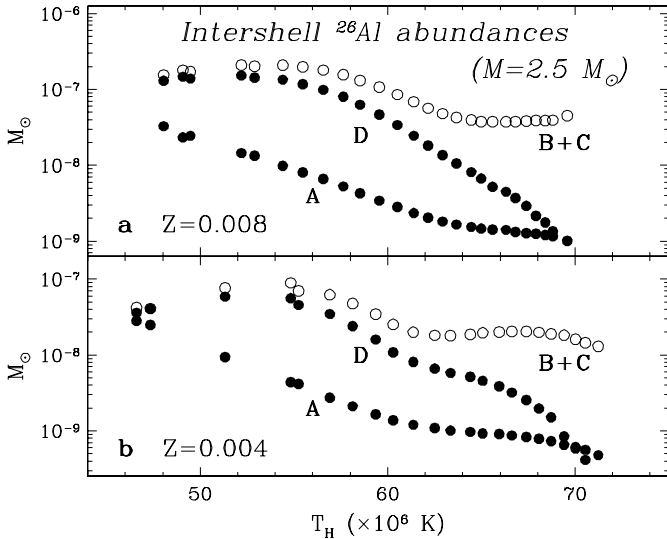


**Fig. 10a and b.** Same as Fig. 9, but for the  $2.5 M_{\odot}$  model stars at metallicities **a**  $Z = 0.008$  and **b**  $Z = 0.004$ .

dance enhancement. What fraction of  $^{26}\text{M}_D$  is actually mixed into the envelope depends on the 3DUP efficiency. This is analyzed in Sect. 5.

**NACRE reaction rates** The standard models presented in this paper are performed with the nuclear reaction rates presented in the Appendix. After those lengthy calculations were concluded, new rates became available by the NACRE compilation. In order to analyze the impact of those new rates on the  $^{26}\text{Al}$  predictions in our AGB model stars, the 22nd interpulse – 23rd pulse sequence of the  $2.5 M_{\odot}$ ,  $Z = 0.018$  star is recomputed using the NACRE rates. The intershell abundance profiles at the end of that interpulse are shown in Fig. 12, which are directly comparable with Fig. 7. As far as  $^{26}\text{Al}$  is concerned, three important conclusions are drawn:

- 1) the amount of  $^{26}\text{Al}$  produced by the HBS is higher with the new rates than with the old ones ( $5 \times 10^{-5}$  mass fraction instead of  $3 \times 10^{-5}$  in the models displayed in Figs. 12 and 7, respectively). This is due, on the one hand, to the lower  $^{26}\text{Al}$  destruction by p-captures and, on the other hand, to a leakage from the Ne–Na to the Mg–Al chain through  $^{23}\text{Na}(p, \gamma)^{24}\text{Mg}$ . The resulting  $^{24}\text{Mg}$  destruction is well visible in Fig. 12. Those features are confirmed by the parametric H-burning calculations presented in the appendix, which further reveal that the amount of  $^{26}\text{Al}$  produced with NACRE is 5 (20) times higher than with the old rates at  $T_H = 70 \times 10^6 \text{ K}$  ( $80 \times 10^6 \text{ K}$ );
- 2) the amount of secondary  $^{13}\text{C}$  predicted by the CNO cycles is lower by almost a factor of two with the new rates compared with the old ones (Appendix A of M99). As a result, less  $^{26}\text{Al}$  is destroyed by n-captures when  $^{13}\text{C}(\alpha, n)^{16}\text{O}$  is activated;
- 3) the amount of  $^{26}\text{Al}$  destroyed (about 38%) in the 23rd pulse is similar with NACRE and with the old reaction rates.

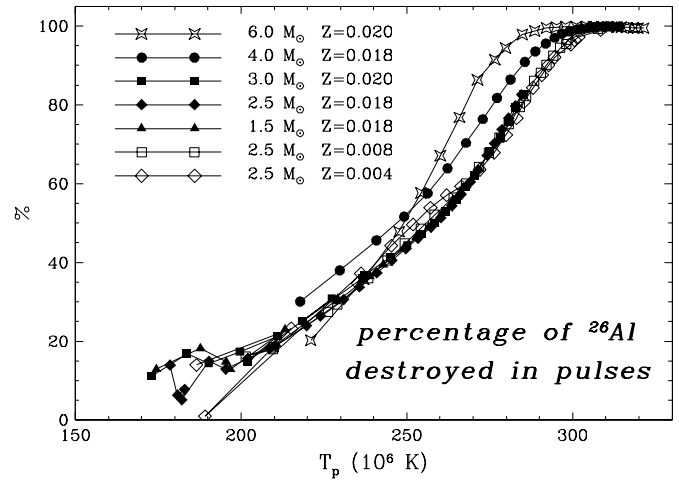


**Fig. 11.** Percentage of  $^{26}\text{Al}$  destroyed in the pulses as a function of pulse temperature for all our model stars as labeled in the figure. It is equal to  $100 * (^{26}\text{M}_{B+C} - ^{26}\text{M}_D) / ^{26}\text{M}_{B+C}$ .

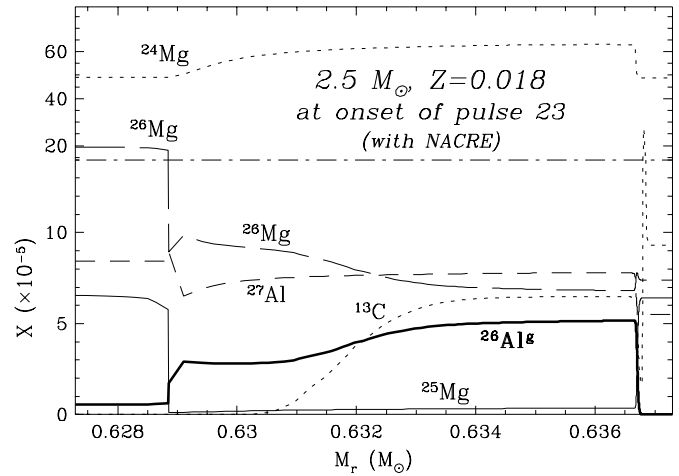


**Fig. 12.** Same as Fig. 7, but with NACRE nuclear reaction rates.

In summary, the NACRE reaction rates lead to higher intershell  $^{26}\text{Al}$  predictions than that predicted with the old reaction rates. Their impact on the surface  $^{26}\text{Al}$  abundance predictions is further analyzed in the next section.

## 5. Mass of $^{26}\text{Al}$ ejected by AGB stars

Because the 3DUP process is not self-consistently obtained in standard models (Sect. 2), we need to simulate the surface abundance evolution with ‘synthetic’ calculations. Those calculations take into account the intershell abundances predicted by the standard models (Sect. 4) and predict the surface abundances pulse after pulse by applying given 3DUP efficiencies as a function of pulse number for each star. The assumptions used in our synthetic calculations are described in Sect. 5.1, and the surface  $^{26}\text{Al}$  abundance predictions analyzed in Sects. 5.2 and 5.3. The mass of  $^{26}\text{Al}$  ejected by our AGB stars are provided in Sect. 5.4.

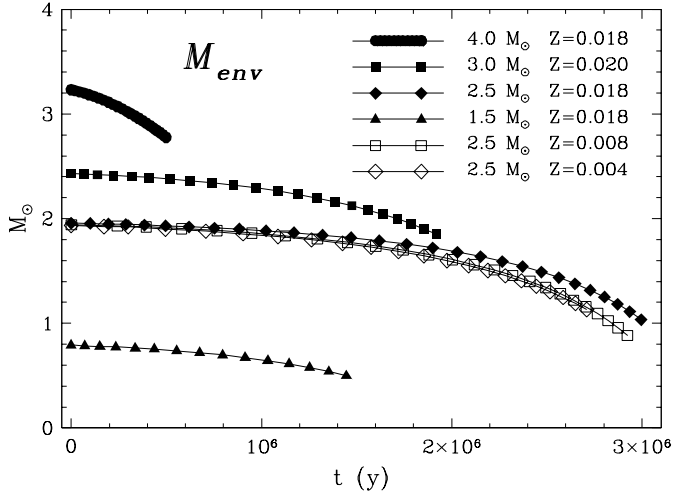


**Fig. 13.** Evolution of the mass of the envelope in each model star as labeled in figure. The time origin is arbitrarily set to that at the first pulse in each star. Each mark locates a pulse time.

### 5.1. Synthetic calculations

We assume in our synthetic calculations that neither the overall structural evolution of the model stars nor the chemical evolution in their intershell layers is affected by the operation of the 3DUPs. The evolution of the envelope’s mass  $M_{env}$  is further assumed to be that predicted by our standard models (Fig. 13). The surface  $^{26}\text{Al}$  abundances are actually not very sensitive on the mass loss rates.

Let us consider the operation of 3DUP after pulse  $i$ . The mass of  $^{26}\text{Al}$  in the envelope after the 3DUP is given by

$${}^{26}M_{env}^i = {}^{26}M_{env}^{i-1} \times \frac{M_{env}^i}{M_{env}^{i-1}} \times e^{-\frac{\Delta t^{i-1}}{\tau}} + \lambda_A^i \times {}^{26}M_A^i + \lambda_D^i \times {}^{26}M_D^i \quad (2)$$

where the exponential factor describes the  $^{26}\text{Al}$  disintegration during the preceding interpulse  $i - 1$  of duration  $\Delta t^{i-1}$  (expressed in years in Eq. 2 and taken from our standard model predictions). The ratio  $M_{env}^i/M_{env}^{i-1}$  takes into account both the mass of  $^{26}\text{Al}$  lost in the wind and the advance of the HBS during interpulse  $i - 1$ .  ${}^{26}M_A^i$  and  ${}^{26}M_D^i$  are the masses of  $^{26}\text{Al}$  in zones  $A$  and  $D$ , respectively, after pulse  $i$ . The dredge-up parameters  $\lambda_A^i$  and  $\lambda_D^i$  define the fraction of zones  $A$  and  $D$ , respectively, which are dredged-up. The evolution of the surface  $^{26}\text{Al}$  mass fraction  $X_s^i(^{26}\text{Al})$  as a function of pulse number is then simply given from Eq. 2 by

$$X_s^i(^{26}\text{Al}) = {}^{26}M_{env}^i / M_{env}^i. \quad (3)$$

In order to evaluate the sensitivity of  $^{26}\text{Al}$  yields on the  $\lambda_A$  and  $\lambda_D$  parameters, three cases are considered, denoted the ‘nominal’, ‘minimal’ and ‘maximal’ cases, each one adopting a specific choice for  $\lambda_A$  and  $\lambda_D$ .

*Nominal case:* The values of  $\lambda_D$  at each pulse of our model stars are taken from ‘non-standard’ model predictions incorpo-

rating diffusive extra-mixing below the envelope. Such a non-standard prescription is able to reproduce self-consistently the 3DUP phenomenon (Mowlavi 1999a). It has been applied to selected afterpulse sequences of each of our stars, providing 3DUP efficiencies as a function of stellar mass, metallicity and pulse number. The details of those 3DUP predictions will be presented in a forthcoming paper (Mowlavi, in preparation). Let us just mention here that

- dredge-up of C-rich material starts at pulse number  $n_{dup} = 5, 14$  and  $18$  in the  $4, 3$  and  $2.5 M_\odot$ , respectively, at solar metallicity, and at  $n_{dup} = 10$  and  $7$  in the  $2.5 M_\odot$  star at  $Z = 0.008$  and  $0.004$ , respectively. No 3DUP is obtained in the  $1.5 M_\odot$  star up to the 16th pulse computed so far;
- the 3DUP efficiency increases during the first dredge-ups almost linearly with core mass, but is reduced at more advanced pulses due to the effect of mass loss.

The value of  $\lambda_A$  is arbitrarily assumed to increase linearly in the nominal case, from 0 at the first pulse to 1 at pulse number  $n_{dup}$  where 3DUP starts to operate<sup>3</sup>.

In order to evaluate the sensitivity of  $^{26}\text{Al}$  yields on the  $\lambda_A$  and  $\lambda_D$  laws adopted in the nominal case, two other cases are considered, providing upper and lower limits of those yields.

*Minimal case:* We assume that no material from zone  $A$  is dredged-up ( $\lambda_A = 0$ ) until the operation of 3DUP (at pulse  $n_{dup}$ ), after which  $\lambda_A = 1$ .  $\lambda_D$ , on the other hand, is taken from our model predictions as in the nominal case. This case provides a lower limit to the  $^{26}\text{Al}$  yields.

*Maximal case* An upper limit for the yields is given by assuming that maximum 3DUP efficiency is achieved from the very first pulse on. The maximum efficiency expected during a 3DUP event is derived from the analysis of Mowlavi (1999a). If we consider the classical 3DUP efficiency parameter  $\lambda = M_{dup}/\Delta M_c$ , which compares the mass  $M_{dup}$  of C-rich material dredged-up to the core mass increase  $\Delta M_c$  during the preceding interpulse phase<sup>4</sup>, then  $\lambda$  asymptotically reaches the value of one after a sufficient number of pulses (in the absence of mass loss). We thus take in the maximal case  $\lambda = 1$ ,  $\lambda_D$  being then given by

$$\lambda_D^i = \lambda \times \Delta M_c^{i-1} / M_D^i. \quad (4)$$

$\lambda_A$  is of course always taken equal to one in this maximal case.

<sup>3</sup> In the  $1.5 M_\odot$  star for which no 3DUP is predicted to occur up to the 16th computed pulse, we nevertheless assume in the nominal case that  $\lambda_A$  increases linearly from zero at the first pulse to one at  $n_{dup} = 16$ .

<sup>4</sup> A value of  $\lambda < 1$ , for example, means that more mass is added to the core by the HBS during the interpulse phase than what is dredged-up during the afterpulse phase, leading to a net increase of the core mass pulse after pulse. A value of  $\lambda > 1$ , on the other hand, results in a decrease of the core mass pulse after pulse, while  $\lambda = 1$  means a constant core mass at each pulse.

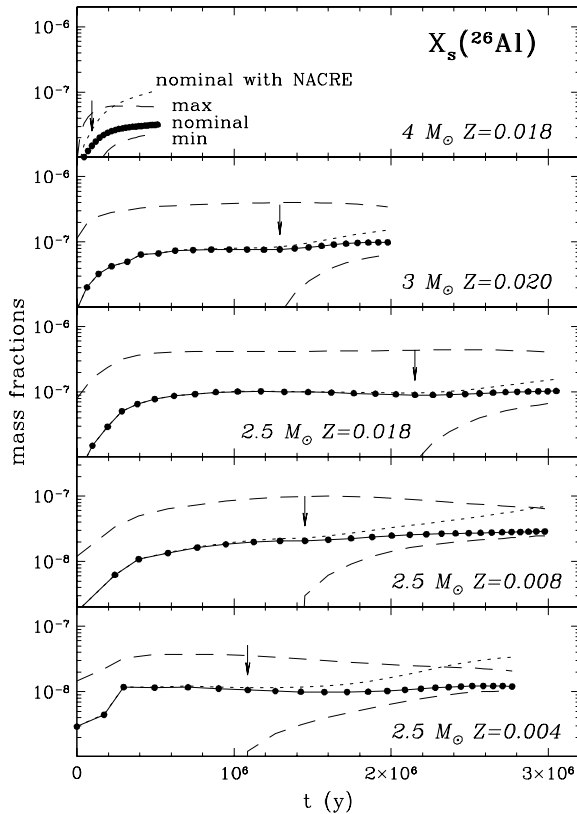


**Fig. 14.** Surface  $^{26}\text{Al}$  abundance evolution predicted by our synthetic calculations. The solid lines with filled circles represent the nominal case 3DUP efficiencies predicted by AGB model calculations, and the dashed lines the minimal and maximal cases defined in the text (Sect. 5). The dotted lines represent predictions in the nominal case, but with NACRE reaction rates (Sect. 5.2). The time origin is set at the first pulse for each star. The arrow in each panel indicates the time from which on dredge-up of C-rich material from zone  $D$  is predicted to start.

### 5.2. $^{26}\text{Al}$ surface abundances

The surface  $^{26}\text{Al}$  abundance evolution predicted by our synthetic calculations in each of the three cases defined in Sect. 5.1 is shown in Fig. 14 for several of our model stars. The nominal case is represented by the solid lines connecting filled circles, and the minimal and maximal cases by the dashed lines respectively below and above the nominal predictions. The surface  $^{26}\text{Al}$  abundances  $^{26}X_s$  at the last computed models of each of our stars are summarized in Table 2 for the three cases (Columns 7 to 9).

In the nominal case, the surface  $^{26}\text{Al}$  abundance increases rapidly up to  $1\text{--}2 \times 10^{-7}$  mass fractions during the first pulses due to the mixing of material from zone  $A$ . It would then decrease slightly with time due to  $\beta$ -decay in the absence of 3DUP. The occurrence of 3DUP (marked by an arrow in Fig. 14), however, brings fresh  $^{26}\text{Al}$  from zone  $D$  to the surface. It keeps  $^{26}X_s$  roughly constant with time to about  $10^{-7}$  mass fractions in  $2.5\text{--}3 M_\odot$  solar metallicity stars. In the  $4 M_\odot$  star,  $^{26}X_s$  is about three times lower due to its massive envelope (but see predictions with the NACRE reaction rates below). The case of the  $6 M_\odot$

star, on the other hand, is treated separately in Sect. 5.3 due to the high temperatures reached at the bottom of its envelope.

In the minimal case,  $^{26}\text{Al}$  pollutes the stellar envelope only after the onset of 3DUP from zone  $D$ . Fig. 14 shows that the minimal case (lower dashed lines) converges to the nominal case after a sufficient number of 3DUPs.

In the maximal case, the predicted surface  $^{26}\text{Al}$  abundances are always about a factor of 2 to 4 higher than in the nominal case. This is of course due to the higher contribution of zone  $D$  to the surface abundance enhancements.  $^{26}X_s$  reaches about  $4 \times 10^{-7}$  mass fractions in the  $2.5\text{--}3 M_\odot$  stars.

The  $^{26}X_s^{\text{max}}/^{26}X_s^{\text{min}}$  ratio between the maximal and minimal cases is given in Table 2 (10th column) for the last computed pulse of each of our stars. The uncertainty is seen to lie between a factor of 2 to 6, depending on the number of 3DUPs experienced by the star. The more the number of 3DUPs, the better the predictions. We thus consider a factor of three uncertainty on our  $^{26}X_s$  predictions in the nominal case as reasonable. We further note that 3DUP is more efficient in low-metallicity stars, which translates in lower uncertainties in their surface  $^{26}\text{Al}$  abundance predictions.

*Predictions with NACRE* The new NACRE reaction rates lead to higher  $^{26}\text{Al}$  intershell abundances than those predicted from the rates used in our models (Sect. 4). We can estimate the surface  $^{26}\text{Al}$  abundances which would result from the NACRE reaction rates by considering that the intershell  $^{26}\text{Al}$  abundance is very well correlated with the HBS temperature. The parametric nucleosynthesis calculations presented in the Appendix, performed once with the rates used in our models and once with the NACRE ones, provide the  $^{26}X_{\text{nacre}}/^{26}X$  factor (Fig. A.2b) by which our intershell  $^{26}\text{Al}$  abundances must be multiplied in order to obtain the intershell abundances expected with NACRE. The resulting  $^{26}\text{Al}$  surface abundance evolution in the nominal case is shown by the dashed lines in each panel of Fig. 14. As expected from the parametric calculations (Fig. A.2b), there is a significant difference between the predictions with NACRE and with the old rates only in massive and low-metallicity stars (i.e. for HBS temperatures above  $\sim 70 \times 10^6$  K). For those stars,  $^{26}X_s$  can be three times higher with NACRE than with the old rates<sup>5</sup>. But it has only a slight impact on solar metallicity stars.

The conclusions drawn in Sect. 6 from our predictions at solar metallicity are thus basically not affected by the new NACRE reaction rates.

### 5.3. Hot bottom burning

Massive AGB stars ( $M \gtrsim 4 M_\odot$  at solar metallicity) are characterized by temperatures  $T_{\text{env},b}$  at the base of their convective envelope exceeding  $50 \times 10^6$  K. As a result the main modes

<sup>5</sup> In our estimation of the impact of NACRE reaction rates on the surface  $^{26}\text{Al}$  abundances, we neglect the fact that NACRE also predicts lower intershell  $^{13}\text{C}$  abundances (Sect. 4). The NACRE predictions for  $^{26}X_s$  would thus even be slightly higher than shown by the dotted lines in Fig. 14.

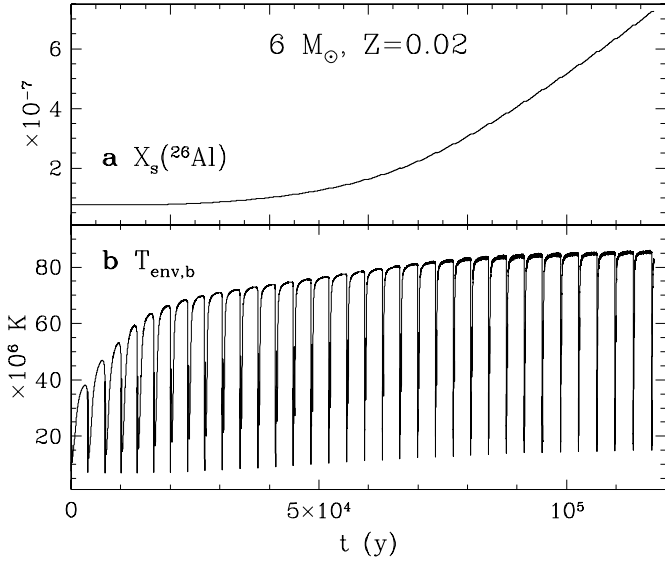


**Fig. 15a and b.** Evolution of: **a** the abundance of  $^{26}\text{Al}$  (in mass fractions) at the surface of the  $6 M_{\odot}$  model star of solar metallicity, **b** the temperature at the bottom of the convective envelope. The time origin is set at the first pulse. For information, the number of pulses calculated in this model star amounts to thirty four.

of H-burning are operating at the base of their envelope (process called hot bottom burning, HBB), and directly modify their surface abundances without requiring any 3DUP process. The  $^{26}\text{Al}$  surface abundance, in particular, is strongly affected by that process. The abundance prediction in our  $6 M_{\odot}$  star of solar metallicity is displayed in Fig. 15a. It is directly taken from our AGB model calculations without invoking any 3DUP process.  $^{26}\text{Al}$  production is seen to be very efficient, reaching surface mass fractions exceeding those predicted in lower-mass AGB stars by the 3DUP process. Indeed,  $^{26}\text{X}_s$  abundances exceeding  $5 \times 10^{-7}$  are easily predicted in those massive AGB models, and values above  $10^{-6}$  seem very realistic. Given the high mass of their envelope (about  $5 M_{\odot}$  for the  $6 M_{\odot}$  star), those stars thus constitute efficient  $^{26}\text{Al}$  production sites. Their possible contribution to the galactic  $^{26}\text{Al}$  abundance is analyzed in Sect. 6.

The influence of the NACRE reaction rates is expected to be small. This is due to the fact that, even though  $T_{\text{env},b}$  reaches  $80 \times 10^6$  K, the effective reaction rate in the envelope is an average (with respect to mass) over the whole convective zone.

#### 5.4. $^{26}\text{Al}$ ejected by AGB stars

We consider a simplified model in which the AGB star smoothly loses mass at a rate  $\dot{M}(M, Z, t)$  which depends on the initial mass  $M$ , metallicity  $Z$  and age  $t$  of the star, until a violent superwind sets in at time  $t_{\text{PN}}$  of planetary nebula (PN) formation and ejects ‘instantaneously’ the remaining stellar envelope’s mass  $M_{\text{env}}(M, Z, t_{\text{PN}})$ <sup>6</sup>.  $\dot{M}(M, Z, t)$  is taken from our model predictions (Sect. 2).

<sup>6</sup> The up to few 10 000 years separating the superwind ejection and the PN formation is negligible given the decay lifetime of  $^{26}\text{Al}$ . Also,

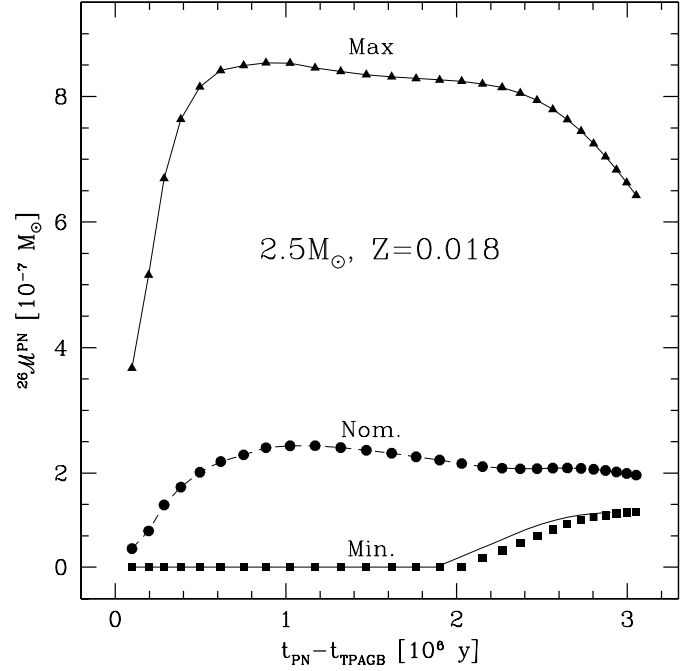


**Fig. 16.** Mass  $^{26}\mathcal{M}^{\text{PN}}(M, Z)$  of  $^{26}\text{Al}$  present in the circumstellar medium right after envelope’s ejection for the  $2.5 M_{\odot}$  stellar model at solar metallicity as a function of the age  $t_{\text{PN}}$  at which the planetary nebula forms. The time origin is set at the onset of the first thermal pulse. Predictions are given for the three cases (minimal, nomimal and maximal) described in Sect. 5.1. The filled points are located at pulse times (beginning at the second pulse).

Let us first consider the mass  $^{26}\mathcal{M}^{\text{AGB}}(M, Z, t)$  of  $^{26}\text{Al}$  present in the circumstellar medium of an AGB star at an age  $t$ . It is given by

$$^{26}\mathcal{M}^{\text{AGB}}(M, Z, t) = \int_{t_{\text{TP}}}^t {}^{26}\text{X}_s(M, Z, t') |\dot{M}(M, Z, t')| e^{-\frac{t-t'}{\tau}} dt', \quad (5)$$

where  $t_{\text{TP}}$  is the stellar age at the onset of the first pulse on the AGB. The amount  $^{26}\mathcal{M}^{\text{AGB}}(M, Z, t_{\text{PN}})$  of  $^{26}\text{Al}$  present in the wind of the end of the AGB lifetime, for example, is given in Columns 11 to 13 of Table 2.

The mass  $^{26}\mathcal{M}^{\text{PN}}(M, Z)$  of  $^{26}\text{Al}$  present in the circumstellar medium right after envelope’s ejection, on the other hand, is given by

$$^{26}\mathcal{M}^{\text{PN}}(M, Z) = {}^{26}\mathcal{M}^{\text{AGB}}(M, Z, t_{\text{PN}}) + {}^{26}\text{X}_s(M, Z, t_{\text{PN}}) M_{\text{env}}(M, Z, t_{\text{PN}}). \quad (6)$$

The first term of the right hand side accounts for the mass of  $^{26}\text{Al}$  present in the wind just prior to the envelope’s ejection and the second term accounts for the mass of  $^{26}\text{Al}$  ejected by the superwind. We can get a rough estimate of  $^{26}\mathcal{M}^{\text{PN}}$  for 2–3  $M_{\odot}$  solar metallicity stars by neglecting, as a first approximation, their wind contribution

we are not concerned here whether the PN actually becomes visible or not.

**Table 2.** Several predictions of our model stars of mass  $M$  and metallicity  $Z$  given in the first two columns. Column 3: age of the star at the first thermal pulse on the AGB. Column 4: total number of computed pulses. Column 5: surface luminosity at the last computed pulse. Column 6: duration of the thermal pulse phase from the first pulse to the last computed one. Columns 7–9:  $^{26}\text{Al}$  surface mass fraction predicted by our synthetic calculations at the last computed pulse in the minimal (Column 7), nominal (8) and maximal (9) cases defined in Sect. 5.1. Column 10 gives the ratio between the surface  $^{26}\text{Al}$  abundance predicted in the maximal and minimal cases. Columns 11–13: mass of  $^{26}\text{Al}$  predicted in the wind of the AGB star at the last computed pulse in the minimal (Column 11), nominal (12) and maximal (13) cases. Columns 14–15: mass of  $^{26}\text{Al}$  predicted in the circumstellar medium after ejection of the stellar envelope at the last computed pulse in the minimal (Column 14), nominal (15) and maximal (16) cases. The figures in brackets concern predictions by hot bottom burning.

$M$ ( $M_{\odot}$ )	$Z$	$t_{TP}$ ( $10^6$ y)	$n_p$	$L$ ( $L_{\odot}$ )	$\Delta_{TP}$ ( $10^6$ y)	$^{26}X_s$ ( $10^{-7}$ )				$^{26}\mathcal{M}^{AGB}$ ( $10^{-7} M_{\odot}$ )			$^{26}\mathcal{M}^{PN}$ ( $10^{-7} M_{\odot}$ )		
						min	nom	max	$\frac{\max}{\min}$	min	nom	max	min	nom	max
Solar metallicity stars															
6	0.020	73	34	41100	0.1	[7.5]				[0.3]			[35]		
4	0.018	204	25	19500	0.5	0.24	0.34	0.59	2.5	0.1	0.1	0.2	0.7	1.0	1.8
3	0.020	487	23	11600	2.0	0.64	0.99	3.48	5.4	0.1	0.3	1.2	1.3	2.1	7.4
2.5	0.018	818	29	11300	3.1	0.69	1.04	4.03	5.8	0.2	0.5	2.1	0.9	1.5	5.9
1.5	0.018	3037	16	8350	1.5	–	1.75*	12.0	> 10	–	0.3*	1.7	–	1.0*	7.2
Low metallicity stars															
2.5	0.008	741	26	12700	3.0	0.25	0.29	0.65	2.6	0.1	0.2	0.4	0.3	0.4	0.9
2.5	0.004	647	23	12000	2.8	0.10	0.12	0.21	2.1	0.0	0.0	0.1	0.1	0.2	0.3

\* No third dredge-up is predicted in the  $1.5 M_{\odot}$  star up to the last (16th) computed pulse, but we still arbitrarily assume in the nominal case that  $\lambda_A$  increases linearly from zero at the first pulse to one at the 16th pulse.

$^{26}\mathcal{M}^{AGB}(M, Z, t_{PN})$  and by taking  $^{26}X_s(M, Z, t_{PN}) \simeq 10^{-7}$  (Fig. 14) and  $M_{env}(M, Z, t_{PN}) = 1-2 M_{\odot}$ . We then get from Eq. 6  $^{26}\mathcal{M}^{PN}(M, Z) \simeq 1-2 \times 10^{-7} M_{\odot}$ . This rough approximation already provides a good estimate of the mass of  $^{26}\text{Al}$  ejected by  $2-3 M_{\odot}$  solar metallicity stars when compared to the more detailed calculations provided below. Actually the wind contribution never exceeds half of the total ejected mass of  $^{26}\text{Al}$ .

Let us analyze in more details the values obtained for  $^{26}\mathcal{M}^{PN}(M, Z)$  using the surface abundance predictions of Sect. 5.2. The prediction for a  $2.5 M_{\odot}$  solar metallicity star is shown in Fig. 16 as a function of the time  $t_{PN}$  at which the superwind is assumed to occur. It is seen that, in general,  $^{26}\mathcal{M}^{PN}(M, Z)$  does not much depend on the time of PN formation, provided it happens after the occurrence of few dredge-ups. If the evolution is pursued beyond the last computed model,  $^{26}\mathcal{M}^{PN}(M, Z)$  is expected to slightly decrease with time as a result of  $^{26}\text{Al}$  disintegration in the envelope. But the decrease would be slow because of the long  $^{26}\text{Al}$  lifetime relative to the interpulse duration (Fig. 14). Taking  $^{26}\mathcal{M}^{PN}(M, Z)$  at the time of the last computed pulse in each of our stars should thus be fairly representative of the mass of  $^{26}\text{Al}$  ejected by AGB stars at the time of PN formation<sup>7</sup>. Those are listed in the last three columns of Table 2 for the minimal, nominal and maximal cases, respectively. The uncertainty linked to the method used to account for the effects of 3DUP are estimated by comparing the predictions of the minimal and maximal cases. It is seen to amount to a factor of about six between the minimal and maximal cases. Those  $^{26}\mathcal{M}^{PN}(M, Z)$  predictions would be slightly

higher (by a factor of maximum two) if the NACRE reaction rates were used.

Let us now discuss the dependence of  $^{26}\mathcal{M}^{PN}(M, Z)$  on the initial stellar mass and metallicity. The  $2.5 M_{\odot}$  and  $3 M_{\odot}$  stars have comparable yields, and the same is true for the maximal case of the  $1.5 M_{\odot}$  model. The ejected mass of  $^{26}\text{Al}$  seems thus independent of initial stellar mass for low-mass stars. In massive AGB stars,  $^{26}\mathcal{M}^{PN}(M, Z)$  is significantly higher due to the occurrence of HBB. For the  $6 M_{\odot}$  star, for example, the quantity of  $^{26}\text{Al}$  present in the envelope at the last computed model amounts to  $35 \times 10^{-7} M_{\odot}$  (that ejected by the stellar wind up to this stage is negligible, around 1%) and increases by about  $4 \times 10^{-7} M_{\odot}$  per 10 000 years ( $1.5 \times 10^{-7} M_{\odot}$  per pulse, Fig. 15). Our ignorance of the duration of the AGB phase unfortunately prevents us to provide more reliable  $^{26}\text{Al}$  yields for those massive AGB stars. As for the metallicity dependence, the predictions for the  $2.5 M_{\odot}$  stars at different metallicities (Table 2) suggest  $^{26}\mathcal{M}^{PN} \propto (Z/Z_{\odot})^{1.0}$  in the minimal case and about  $^{26}\mathcal{M}^{PN} \propto (Z/Z_{\odot})^{1.6}$  in the nominal and maximal cases. Those results are roughly consistent with other predictions in the literature (Forestini & Charbonnel 1997), obtained with different 3DUP assumptions and nuclear reaction rates.

## 6. Comparison with observations

The most reliable  $^{26}\text{Al}$  abundance observations available at present come from  $^{26}\text{Al}/^{27}\text{Al}$  measurements in meteoritic grains. This is discussed in Sect. 6.1. A direct observation of  $^{26}\text{Al}$  at the surface of an AGB star has possibly been reported in IRC+10216, and is confronted to our predictions in Sect. 6.2. Finally, we estimate the contribution of AGB stars to the interstellar  $^{26}\text{Al}$  enrichment in Sect. 6.3 and discuss the possibility

<sup>7</sup> For the  $2.5$  and  $3 M_{\odot}$  solar metallicity stars, the luminosities reached at the last computed pulse ( $\sim 10^4 L_{\odot}$ , cf. Table 2) are compatible with those characterizing visible PNe.

to observe single AGB stars or planetary nebulae at 1.8 MeV  $\gamma$ -ray in Sect. 6.4.

### 6.1. Meteoritic grains

Some meteoritic grains have isotopic compositions very different from the solar one (see e.g. Bernatowicz & Zinner 1997). These pieces of dust are interpreted as pristine circumstellar material which was present in the proto-solar cloud from which the Solar System formed 4.6 billion years ago and which remained unaltered until the present time. These grains provide a direct access to the circumstellar environment from which they originate, provided that we know around which kind of star they were formed (a question which is far from being resolved). In particular, their isotopic composition gives strong constraints on the nucleosynthetic processes believed to have occurred in their parent star. In this section we briefly discuss the constraints that such meteoritic grains can provide on  $^{26}\text{Al}$  production by AGB stars.

Let us recall that AGB stars are believed to be producers of silicon carbide (SiC) and corundum (also called oxide) grains. We refer to the review by Zinner (1997). In those grains,  $^{26}\text{Al}/^{27}\text{Al}$  ratios much higher than the canonical value of  $5 \times 10^{-5}$  have been measured (Hoppe & Ott 1997; Nittler 1997; Amari 1999).

The SiC grains are divided into six distinct groups, based on the isotopic ratios measured for C, N, Si and Al. The groups are called Mainstream, A, B, X, Y and Z (Hoppe & Ott 1997). The  $^{26}\text{Al}/^{27}\text{Al}$  ratios measured in Mainstream, A and B groups<sup>8</sup> are plotted in Fig. 17 as a function of their  $^{12}\text{C}/^{13}\text{C}$  ratios. Most of the Mainstream grains have  $^{14}\text{N}/^{15}\text{N}$  ratios between 500 and 5000 (the Solar System value is 272). Many of the A+B grains (in particular the A grains) are enriched in  $^{15}\text{N}$ , *i.e.* have  $^{14}\text{N}/^{15}\text{N}$  ratios as low as 5–50.

The predictions from our model calculations in the nominal case (Sect. 5) are also shown in Fig. 17. The initial surface  $^{12}\text{C}/^{13}\text{C}$  ratios are those predicted after the first dredge-up in each star, and range around 18–20 depending on the stellar mass. During the AGB phase, this ratio increases in  $M \lesssim 4 M_{\odot}$  stars as a result of 3DUP of  $^{12}\text{C}$  from the intershell layers to the surface, while it decreases at the surface of massive AGB stars as a result of HBB. The arrows in Fig. 17 indicate the direction of the  $^{12}\text{C}/^{13}\text{C}$  evolution in our models.

At first glance, the  $^{26}\text{Al}/^{27}\text{Al}$  predictions of the  $6 M_{\odot}$  star undergoing HBB look in very good agreement with the isotopic ratios measured in A+B SiC grains. However, AGB stars undergoing HBB (as the  $6 M_{\odot}$  model plotted in Fig. 17) have C/O ratios at their surface inferior to one, and are thus not expected to form SiC grains<sup>9</sup> (which requires a C-rich environment; see, e.g., Lattimer et al. 1978). Moreover massive AGB models fail to

<sup>8</sup> The  $^{12}\text{C}/^{13}\text{C}$  isotopic ratio is in the range [10–100] for ‘mainstream’ grains, [2.5–3] for ‘A’ grains and [3–10] for ‘B’ grains. These three groups contain more than 90% of all the SiC grains.

<sup>9</sup> Massive AGB stars experiencing HBB can actually become carbon stars when mass loss has sufficiently reduced their envelope’s mass (thus quenching off HBB), if dredge-up continues to enrich their surface

explain the nitrogen isotopic ratios measured in A and B grains. From these considerations, one is forced to conclude that A+B grains are most probably not produced around massive AGB stars undergoing HBB!

The  $^{26}\text{Al}/^{27}\text{Al}$  ratio predictions of the  $M \lesssim 4 M_{\odot}$  stars undergoing 3DUP episodes are at the upper limit of the ratios observed in Mainstream grains (predictions from the minimal case would not change much the picture). This means that either standard model predictions are indeed too high for  $^{26}\text{Al}$  production. In that case, the present  $^{26}\text{Al}$  yields from AGB stars might be overestimated. Or it may indicate some constraints on the production of those mainstream grains around AGB stars. In that respect it is important to mention that other characteristic of these grains still point toward an origin around low-mass ( $M < 2 M_{\odot}$ ) AGB stars having undergone extra-mixing processes during the red giant phases (e.g. Wasserburg et al. 1995). We leave this question open, a due discussion of which is beyond the scope of this article.

Finally, oxide grains form in stellar ejecta with  $\text{C/O} < 1$  (e.g. corundum and hibonite grains, Choi et al. 1999; see also the review by Nittler 1997). Oxide grains are divided into four main categories (Groups 1 to 4) depending on their  $^{16}\text{O}/^{17}\text{O}$  and  $^{16}\text{O}/^{18}\text{O}$  ratios. A subset of these grains present  $^{26}\text{Al}$  enrichments with  $^{26}\text{Al}/^{27}\text{Al}$  ratios between 0.0001 and 0.008. Very interestingly, the present models, which are indeed characterized by  $\text{C/O} < 1$ , account well for the mean observed  $^{26}\text{Al}/^{27}\text{Al}$  ratio of 0.0023 characterizing the Group 1 grains and which are believed to have formed around AGB stars. A more thorough study of those grains should be performed by considering all the isotopic ratios (such as the oxygen ones) together. Such a discussion is however also outside the scope of this article.

As a conclusion, a comparison of our predictions with the isotopic ratios in meteoritic grains shows that

- A+B grains, despite showing  $^{26}\text{Al}/^{27}\text{Al}$  and  $^{12}\text{C}/^{13}\text{C}$  ratios compatible with massive AGB model predictions, do most probably not originate from AGB stars;
- Mainstream SiC grains most probably do originate from AGB stars, but models predict too high  $^{26}\text{Al}$  production;
- Group 1 oxide grains show  $^{26}\text{Al}/^{27}\text{Al}$  ratios compatible with AGB model predictions.

### 6.2. IRC+10216

IRC+10216 (CW Leo) is the nearest ( $\sim 120$  pc) and best studied carbon star because of its high infrared and millimetric luminosity. It is believed to be in its finale stage of evolution on the AGB before turning into a post-AGB star. This is evidenced by the presence of a thick multi-shell circumstellar envelope (e.g. Maunon & Huggins 1999) and by a high mass loss rate

with fresh carbon (Frost et al. 1998). The grains formed around those C stars would then display the large  $^{26}\text{Al}/^{27}\text{Al}$  ratios characteristic of HBB (the typical evolutionary time scale of massive AGB stars is some  $10^4$  yr, which prevents noticeable  $^{26}\text{Al}$  disintegration). However, their  $^{12}\text{C}/^{13}\text{C}$  ratio would then be much higher than those measured in A and B grains.

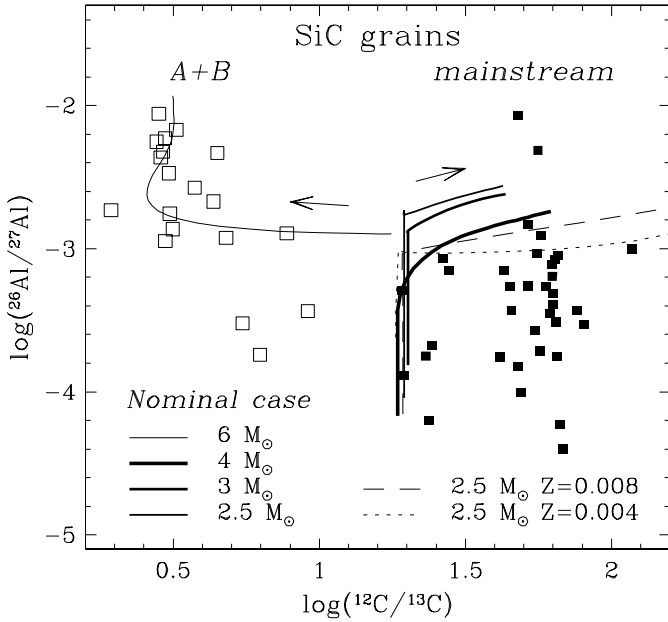


**Fig. 17.** Aluminum and carbon isotopic abundance ratios measured in mainstream (filled squares) and A+B (open squares) SiC grains. AGB model predictions (in the nominal cases) are given for our 2.5 (thin line to the right), 3 (medium thickness line), 4 (thick line) and 6  $M_{\odot}$  (thin line to the left) solar metallicity stars and for the  $Z = 0.008$  (long dashed) and 0.004 (short dashed) 2.5  $M_{\odot}$  stars. The arrows indicate the direction of evolution of the surface abundances in the  $^{12}\text{C}/^{13}\text{C} - ^{26}\text{Al}/^{27}\text{Al}$  diagram during the AGB phase.

of  $\sim 2 \times 10^{-5} M_{\odot} \text{yr}^{-1}$  (e.g. Groenewegen et al. 1998). Near-infrared as well as optical images indeed reveal the birth of a PN around that star (Kastner & Weintraub 1994, Skinner et al. 1998). The luminosity of the central star is estimated to be 10 000–15 000  $L_{\odot}$  (Groenewegen et al. 1998), compatible with values expected at the tip of the AGB for stars with initial masses below about 3  $M_{\odot}$ .

The chemical composition of IRC+10216 points towards an evolved stage on the AGB as well (e.g. Kahane et al. 1988, 1992, 2000). Both the high C/O (of about 1.4 in number, solar = 0.42) and low  $^{35}\text{Cl}/^{37}\text{Cl}$  (of 2.3, solar = 3.1) ratios attest of AGB nucleosynthesis,  $^{12}\text{C}$  being a direct product of He-burning and  $^{37}\text{Cl}$  ( $^{35}\text{Cl}$ ) being enhanced (depleted) by the s-process nucleosynthesis occurring in the HeBS. The ‘low’  $^{12}\text{C}/^{13}\text{C}$  isotopic ratio of  $44 \pm 3$ , combined with  $\text{C}/\text{O} \simeq 1.4$ , further requires the progenitor of IRC+10216 to be a low-mass star<sup>10</sup> ( $M < 2 M_{\odot}$ ).

A direct detection of  $^{26}\text{Al}$  in IRC+10216 has been attempted by measuring the  $^{26}\text{Al}/^{27}\text{Al}$  ratio from AlCl and AlF transition lines (Guélin et al. 1995). The first of these two molecules sets an upper limit of  $^{26}\text{Al}/^{27}\text{Al} < 0.1$ , while the AlF observations would imply  $^{26}\text{Al}/^{27}\text{Al} \simeq 0.04$  if the 234433 MHz transition line used to identify  $^{26}\text{AlF}$  is indeed due to that isotopomer.

<sup>10</sup> In low-mass stars, the surface  $^{12}\text{C}/^{13}\text{C}$  ratio at the onset of the AGB phase is about 10 according to observations of red giants. For an intermediate-mass star, this ratio is about 20 at the start of the AGB (e.g., El Eid 1994), which would imply a  $^{12}\text{C}/^{13}\text{C}$  ratio above 100 when C/O reaches 1.4 on the AGB.

If confirmed, such a high value of  $^{26}\text{Al}/^{27}\text{Al}$  in IRC+10216 would only be compatible, according to our predictions, with a massive AGB star experiencing HBB (low-mass AGB models predict a maximum ratio ten times lower than that measured in IRC+10216, see Fig. 17). This, however, is incompatible with the above-mentioned conclusions of a low-mass progenitor. The fact that  $^{18}\text{O}$  is detected goes also against the operation of HBB, which easily destroys that element.

How can we then reconcile the high  $^{26}\text{Al}/^{27}\text{Al}$  ratio with current  $^{26}\text{Al}$  predictions of low-mass AGB stars? Guélin et al. (1995) invoke the possible dredge-up of  $^{26}\text{Al}$  at the tip of the AGB. At that stage, the envelope’s mass has been much reduced, and  $^{26}\text{Al}$  is less diluted when mixed from the intershell layers into the envelope. This would, in principle, enable to obtain a high  $^{26}\text{Al}/^{27}\text{Al}$  ratio at the stellar surface. However, the 3DUP efficiency is predicted to decrease, according to our current understanding of the 3DUP properties, with the envelope’s mass. The scenario of a 3DUP at the tip of the AGB would thus need to be confirmed by consistent evolutionary AGB models.

The high  $^{26}\text{Al}/^{27}\text{Al}$  ratio observed in IRC+10216, if confirmed, would thus present a new challenge for AGB modelers.

### 6.3. Galactic $^{26}\text{Al}$

In this section we estimate the contribution of AGB stars to the present mass of  $^{26}\text{Al}$  in our Galaxy, and compare it to the 2–3  $M_{\odot}$  estimate deduced from observations at 1.8 MeV. For simplification, we only consider solar metallicity stars and drop in this section the  $Z$  notation in the formulae.

Let us denote by  $\mathcal{N}(M, t)$  the formation rate of stars of initial mass  $M$  (in solar units) in our whole Galaxy  $t$  years ago. The mass of live  $^{26}\text{Al}$  present today due to the contribution of stars of initial mass  $M$  throughout the history of our Galaxy is

$${}^{26}\mathcal{M}^{gal}(M) = \int_{t_{TP}(M)}^{t_{PN}(M)} {}^{26}\mathcal{M}^{AGB}(M, t) \mathcal{N}(M, t) dt \quad (7) \\ + \int_{t_{PN}(M)}^{t_{Gal}} {}^{26}\mathcal{M}^{PN}(M) e^{-\frac{t-t_{PN}(M)}{\tau}} \mathcal{N}(M, t) dt.$$

where  $t_{Gal}$  is the age of our Galaxy. The first term of the right hand side accounts for stars of initial mass  $M$  born between  $t_{TP}$  and  $t_{PN}$  years ago (i.e. which are still in the thermal pulse AGB phase today). Their contribution comes from the wind they currently eject, and is directly given by Eq. 5. The second term of the right hand side of Eq. 7 accounts for all stars of initial mass  $M$  born earlier than  $t_{PN}$  years ago. Their contribution comes from their wind and superwind ejection given by Eq. 6, taking into account the disintegration suffered by that  $^{26}\text{Al}$  from the time of PN ejection  $t_{PN}$  years ago until now. We suppose here that the destruction of  $^{26}\text{Al}$  comes only from its  $\beta^+$ -disintegration. The total mass of live  $^{26}\text{Al}$  present today in our Galaxy due to all stars with masses between  $M_1$  and  $M_2$  is then given by

$${}^{26}\mathcal{M}^{gal}(M_1, M_2) = \int_{M_1}^{M_2} {}^{26}\mathcal{M}^{gal}(M) dM. \quad (8)$$

The stellar formation rate  $\mathcal{N}(M, t)$  is given by

$$\mathcal{N}(M, t) = \Psi(t) \times \Phi(M) \quad (9)$$

where  $\Psi(t)$  is the star formation rate (SFR, expressed here in number of stars per yr in the Galaxy) and  $\Phi(M, t)$  the initial mass function (IMF). We assume that both the SFR and the IMF are time-independent (and drop the  $t$  parameter hereafter).  $\mathcal{N}(M)$  is further normalized to have  $\nu_{SN}$  core collapse supernovae events per century in our Galaxy. Using a Salpeter IMF  $\Phi(M) = M^{-2.35}$ , this leads to

$$\nu_{SN} = 100 \times \Psi \times \int_8^{120} \Phi(M) dM = 4.36 \times \Psi. \quad (10)$$

Using Eqs. 7, 9 and 10, Eq. 8 becomes

$${}^{26}\mathcal{M}^{gal}(M_1, M_2) = \frac{\nu_{SN}}{4.36} \times \int_{M_1}^{M_2} \left[ \int_{t_{TP}(M)}^{t_{PN}(M)} {}^{26}\mathcal{M}^{AGB}(M, t) dt + \int_{t_{PN}(M)}^{t_{Gal}} {}^{26}\mathcal{M}^{PN}(M) e^{-\frac{t-t_{PN}(M)}{\tau}} dt \right] M^{-2.35} dM \quad (11)$$

We evaluate Eq. 11 for mass intervals [1–2], [2–2.8], [2.8–3.5], [3.5–5], [5–7]  $M_\odot$ , taking in each of them constant  ${}^{26}\mathcal{M}^{AGB}$ ,  ${}^{26}\mathcal{M}^{PN}$ ,  $t_{PN}$  and  $\Delta_{TP} = t_{PN} - t_{TP}$ . All these quantities can be deduced from the values given in Table 2 at 1.5, 2.5, 3, 4 and 6  $M_\odot$ , respectively. Adopting  $\nu_{SN} = 3$  supernovae per century, Eq. 11 yields a *contribution of 0.2  $M_\odot$  of  ${}^{26}\text{Al}$  from AGB stars*. Roughly half of it is provided by massive AGB stars ( $M \geq 5 M_\odot$ ). Actually,  ${}^{26}\mathcal{M}^{gal}(1, 8)$  varies from 0.01 to 0.4  $M_\odot$  depending on the 3DUP assumptions made in evaluating  ${}^{26}\mathcal{M}^{AGB}(M, t)$  and  ${}^{26}\mathcal{M}^{PN}(M)$  and on  $\Delta t_{TP}$ .

Unless the supernova rate is greatly underestimated, even the highest value represents only one fifth at most of the total  ${}^{26}\text{Al}$  believed to be present in the Galaxy today. Such a result discards AGB stars as an important source of Galactic  ${}^{26}\text{Al}$ , a fact in agreement with the morphological analysis of the Galaxy at 1.8 MeV obtained by Comptel (Knödlseeder 1999). Let us however emphasize that low mass AGB stars could be responsible for a 1.8 MeV emission from extended sources with low surface brightness, which may not be recorded by COMPTEL (see Naya et al. 1998). In that case, the present results give an upper limit for such an emission from AGB stars of the order of 0.4  $M_\odot$ .

#### 6.4. Single source detection at 1.8 MeV: perspectives with INTEGRAL

It is instructive to analyze the perspectives of detecting the 1.8 MeV emissivity of single AGB stars and/or PNe by the future International Gamma Ray Laboratory (INTEGRAL) satellite.

##### 6.4.1. AGB stars

The mass of live  ${}^{26}\text{Al}$  present around a given AGB star (i.e. in its wind ejecta) of initial mass  $M$  and metallicity  $Z$  is given by

the quantity  ${}^{26}\mathcal{M}^{AGB}(M, Z)$  evaluated in Sect. 5.4 and given in Table 2 for our model stars. It amounts to few  $10^{-8} M_\odot$  in the nominal cases of solar metallicity stars.

The maximum distance  $D_{max}$  at which a given mass  ${}^{26}\mathcal{M}$  of  ${}^{26}\text{Al}$  can be detected as a point source by the future INTEGRAL mission is given by

$$D_{max} = 14 \sqrt{{}^{26}\mathcal{M}} \quad (12)$$

where  $D_{max}$  is expressed in parsec and  ${}^{26}\mathcal{M}$  in units of  $10^{-7} M_\odot$ . We assume that the minimum flux detectable by INTEGRAL at 1.8 MeV is  $6 \times 10^{-6}$  photons  $\text{cm}^{-2} \text{sec}^{-1}$  (cf. Winkler 1997; a decrease of this threshold by a factor of ten would increase  $D_{max}$  by a factor of  $\sqrt{10} = 3.16$ ).

The  ${}^{26}\text{Al}$  predicted in the wind ejecta of a 2.5  $M_\odot$  AGB star of solar metallicity, for example, would be detectable by INTEGRAL up to 6 (minimal), 10 (nominal) or 20 (maximal case) pc. If we assume a stellar density of about one star per  $\text{pc}^3$  in the solar neighborhood, then there are  $N_* \sim 4200$  (33500) stars in a sphere of radius equal to 10 pc (20 pc) around the sun. The number  $N_{TP}$  of AGB stars in the thermal pulse phase is roughly given by

$$N_{TP} = N_* \times \frac{\int_1^4 \Delta t_{TP} \times \Phi(M) dM}{\int_{0.08}^{120} t_{life}(M) \times \Phi(M) dM} \quad (13)$$

where  $t_{life}(M)$  is the lifetime of a star of initial mass  $M$ . Taking roughly  $\Delta_{TP} = 2 \times 10^6$  y, Eq. 13 leads to  $N_{TP} = 0.02$  and 0.2 in the nominal and maximal cases, respectively. The probability to find a thermally pulsing AGB star close enough to our sun for its  ${}^{26}\text{Al}$  emission line to be detected by INTEGRAL is thus very weak.

What about IRC 10216 (see Sect. 6.2)? At its assumed distance of 120 pc, the minimum amount of  ${}^{26}\text{Al}$  required for a detection by INTEGRAL is  $53 \times 10^{-7} M_\odot$ . Assuming  ${}^{26}\text{Al}/{}^{27}\text{Al}=0.04$  as suggested by the observations of Guélin et al. (1995) and a solar abundance of  ${}^{27}\text{Al}$ , the  ${}^{26}\text{Al}$  surface mass fraction is  $2 \times 10^{-6}$ . For IRC 10216 to be detectable by INTEGRAL, the star must thus have ejected 2.6  $M_\odot$  of envelope during a time interval short compared to the disintegration time of  ${}^{26}\text{Al}$ . The mass loss rate of  $2 \times 10^{-5} M_\odot$  per year is actually compatible with that requirement, so that IRC 10216 could be an interesting candidate to observe with INTEGRAL. Given the disagreement between observations and predictions for that star (see Sect. 6.2), the possible detection of  ${}^{26}\text{Al}$  around IRC+10216 by INTEGRAL would provide an important piece of information to better understand that star, and the nucleosynthesis in AGB stars in general.

##### 6.4.2. Planetary nebulae

PNe may represent more favorable candidates than AGB stars for direct  ${}^{26}\text{Al}$  detection because the mass  ${}^{26}\mathcal{M}^{PN}(M, Z)$  of live  ${}^{26}\text{Al}$  predicted around those objects is higher than around AGB stars (Sect. 5.4). Our models predict 1–2  $\times 10^{-7} M_\odot$  of  ${}^{26}\text{Al}$  around typical PNe with low-mass solar metallicity progenitors (Table 2). A PN formed from an initial 2.5  $M_\odot$  AGB

star of solar metallicity, for example, could be observed up to a distance of 13 (minimal), 17 (nominal) or 34 (maximal case) pc.

Planetary nebulae resulting from a massive AGB star progenitor would represent the most promising case. A  $6 M_{\odot}$  AGB star ejecting its entire envelope content of  $^{26}\text{Al}$  (i.e.  $35 \times 10^{-7} M_{\odot}$ , see Table 2), for example, would be detectable by INTEGRAL up to a distance of 82 pc. This represents the distance at which the nearest PN, NGC 7293, is observed ( $\gtrsim 80$  pc in the catalogue of Planetary Nebulae of Acker et al. 1992). Of course, the probability that those near PNe are massive AGB remnants is weak, were it only because the IMF statistically favors low-mass stars.

## 7. Conclusions

Our model calculations confirm that  $^{26}\text{Al}$  can be efficiently produced in the intershell layers of AGB stars and brought to the surface by the operation of successive 3DUP events. It reveals in particular the importance of the region which emerges from each pulse (zone called *D* in this paper) and which contains a potential reservoir of  $^{26}\text{Al}$  available for 3DUP, at least when the pulse temperature does not exceed  $300 \times 10^6$  K (at which point the neutrons released by  $^{22}\text{Ne} (\alpha, n) ^{25}\text{Mg}$  lead to efficient  $^{26}\text{Al}$  destruction). This condition is typically fulfilled during the first twenty pulses or so of  $2.5 M_{\odot}$  solar metallicity stars. Massive AGB stars, on the other hand, are efficient  $^{26}\text{Al}$  production factories through hot bottom burning.

Abundance predictions at the surface of AGB stars, in the wind of AGB stars and in the circumstellar environment of planetary nebulae are given in Table 14 for three cases named minimal, nominal and maximal. The definition of those cases depends on the adopted dredge-up efficiency as a function of pulse number, as described in Sect. 5.1. Despite the fact that we are using 3DUP efficiencies predicted by model calculations, the uncertainties affecting the  $^{26}\text{Al}$  yields are still high, up to almost an order of magnitude, due to the uncertainties affecting dredge-up predictions. This uncertainty decreases after the occurrence of a sufficient number of 3DUP events. The typical surface  $^{26}\text{Al}$  abundance is of the order of  $10^{-7}$ , and the mass of  $^{26}\text{Al}$  ejected into space at the time of planetary nebula formation  $1\text{--}2 \times 10^{-7} M_{\odot}$  for low-mass stars of solar metallicity.

Observational data for  $^{26}\text{Al}$  include the  $^{26}\text{Al}/^{27}\text{Al}$  abundance ratios inferred in meteoritic grains, the  $^{26}\text{Al}$  abundance possibly measured at the surface of the carbon star IRC+10216, and the mass of live  $^{26}\text{Al}$  present in our Galaxy today. Meteoritic grains, with inferred  $^{26}\text{Al}/^{27}\text{Al}$  ratios ranging from  $\sim 10^{-4}$  to  $10^{-2}$ , are so far the best candidates to confront our predictions with. Ironically, standard models of low-mass AGB stars predict  $^{26}\text{Al}$  abundances which are very high compared to those measured in most mainstream SiC grains (the predicted  $^{26}\text{Al}/^{27}\text{Al}$  ratios are compatible with the highest values measured in those grains). If our low-mass yields are indeed too high, then the mass of live  $^{26}\text{Al}$  predicted to be present in the Galaxy today as a result of those AGB stars, which amounts to  $\sim 0.1 M_{\odot}$ , would also be too high. The contribution of massive AGB stars to the current galactic  $^{26}\text{Al}$  amounts also to  $\sim 0.1 M_{\odot}$ . The high

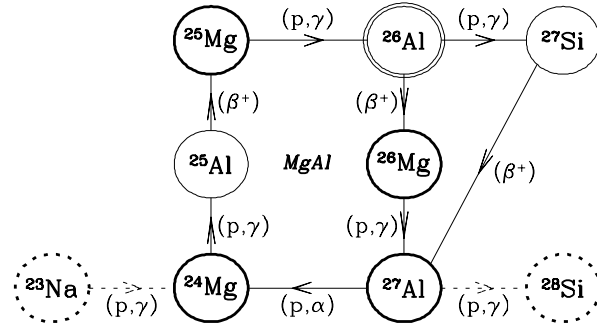


**Fig. A.1.** Reactions of the Mg–Al chain. Stable nuclides are enclosed in thick circles. The possible leakages in and out of the chain are represented by the dashed lines.

$^{26}\text{Al}/^{27}\text{Al}$  ratio predicted at the surface of those massive stars seem compatible with those measured in A+B grains. However, due consideration of other isotopic ratios indicates that those grains do most probably not originate from massive AGB stars. Finally, we note that our abundance predictions cannot explain the high  $^{26}\text{Al}/^{27}\text{Al}$  ratio of 0.04 possibly observed in IRC+1016. A confirmation of IRC+1016 observations is thus highly desirable.

The probability to find a thermally pulsing AGB star close enough ( $\lesssim 20$  pc) to our sun to detect its 1.8 MeV emission as a point source with INTEGRAL seems rather unlikely according to our predictions. If we accept the  $^{26}\text{Al}$  abundance measured at the surface of IRC+10216, then that star may be a good candidate if it has ejected  $\sim 2 M_{\odot}$  of its envelope by a superwind. A detection of a PN as a single source, on the other hand, is possible up to  $\sim 80$  pc if it originates from a massive AGB progenitor. It is however unlikely, according to current PNe catalogues, to find such a PNe so close to the sun.

*Acknowledgements.* We thank Dr. Sachiko Amari for having kindly sent us in electronic format the table of the isotopic abundances in SiC meteoritic grains.

## Appendix A: the Mg–Al mode of hydrogen burning

### The Mg–Al chain

The reactions involved in the Mg–Al chain of hydrogen burning are shown in Fig. A.1. The ground state  $^{26}\text{Al}^g$  (half lifetime  $t_{1/2} = 7.40 \times 10^5$  yr) and the isomeric state  $^{26}\text{Al}^i$  ( $t_{1/2} = 6.35$  sec) of  $^{26}\text{Al}$  are considered as two distinct species. They can either  $\beta$ -decay into  $^{26}\text{Mg}$  or capture protons to form  $^{27}\text{Si}$  which decays into  $^{27}\text{Al}$ . We refer to Arnould et al. (1999) for a further description of the Mg–Al chain.

The Mg–Al reaction rates adopted in our standard model calculations are listed in Table A.1. They are the same as in Mowlavi (1995), except for p captures on  $^{23}\text{Na}$ ,  $^{25}\text{Mg}$  and  $^{26}\text{Al}^g$ .

In order to analyze the sensitivity of  $^{26}\text{Al}$  production on the temperature at which H burns, parametric nucleosynthesis calculations are performed by assuming a constant temperature during the entire H-burning. The Mg–Al yields at hydrogen exhaustion are displayed in Fig. A.2a (solid lines) as a function

**Table A.1.** Reaction rates used in our models for those reactions involved in the Mg–Al chain of H–burning.

Reaction	reference
$^{23}\text{Na} (p, \gamma) ^{24}\text{Mg}$	El Eid & Champagne (1995) <sup>a</sup>
$^{24}\text{Mg} (p, \gamma) ^{25}\text{Al}$	CF88
$^{25}\text{Mg} (p, \gamma) ^{26}\text{Al}^g$	Coc et al. (1995)
$^{25}\text{Mg} (p, \gamma) ^{26}\text{Al}^i$	Coc et al. (1995)
$^{26}\text{Mg} (p, \gamma) ^{27}\text{Al}$	Iliadis et al. (1990) <sup>a</sup>
$^{26}\text{Al}^g (p, \gamma) ^{27}\text{Si}$	Coc et al. (1995) <sup>a</sup>
$^{26}\text{Al}^i (p, \gamma) ^{27}\text{Si}$	CF88
$^{27}\text{Al} (p, \alpha) ^{24}\text{Mg}$	Timmermann et al. (1988) <sup>a</sup> + Champagne et al. (1988) <sup>b</sup>
$^{27}\text{Al} (p, \gamma) ^{28}\text{Si}$	Timmermann et al. (1988) <sup>a</sup>

<sup>a</sup> Geometric average between lower and upper limits

<sup>b</sup> Resonant contributions from Champagne et al. (1988)

of the burning temperature. The main features concerning  $^{26}\text{Al}$  production are:

- $^{26}\text{Al}$  is efficiently produced at temperatures above  $\sim 35 \times 10^6$  K from the conversion of  $^{25}\text{Mg}$  by proton capture. The  $^{26}\text{Al}$  abundance at the end of H–burning reaches values of  $5 \times 10^{-5}$  mass fractions.
- $^{26}\text{Al}$  destruction by p–captures becomes noticeable at temperatures exceeding  $\gtrsim 55 \times 10^6$  K. At  $T = 65 \times 10^6$  K, the  $^{26}\text{Al}$  abundance drops to about  $3 \times 10^{-5}$  mass fractions. The  $^{26}\text{Al}$  destruction is accompanied by a concomitant  $^{27}\text{Al}$  abundance increase.
- The abundant  $^{24}\text{Mg}$  begins to burn through p–capture reactions at  $T \simeq 65 \times 10^6$  K. This replenishes the whole Mg–Al chain.  $^{26}\text{Al}$ , in particular, keeps an abundance of  $3\text{--}4 \times 10^{-5}$  mass fractions up to  $75 \times 10^6$  K.

In summary, the  $^{26}\text{Al}$  abundance at the end of H–burning reaches values between  $3$  and  $5 \times 10^{-5}$  mass fractions in the whole temperature range from  $35$  to  $77 \times 10^6$  K. The situation is even better with the new NACRE reaction rates, at least regarding  $^{26}\text{Al}$ , as shown below.

#### NACRE reaction rates

The effects of the new NACRE reaction rates on the Mg–Al yields at the end of H–burning are shown in dashed lines in Fig. A.2a. Those yields are seen to be similar to the ones obtained with the old reaction rates at temperatures below  $\sim 55 \times 10^6$  K (except for  $^{25}\text{Mg}$  which is not very abundant anyway). At higher temperatures, however, significant differences exist due to two main features.

First,  $^{26}\text{Al} (p, \gamma) ^{27}\text{Si}$  is slower with NACRE than with the rates from Coc et al. (1995).  $^{26}\text{Al}$  is consequently less destroyed, leading to higher  $^{26}\text{Al}$  and lower  $^{27}\text{Al}$  abundances. Secondly,  $^{24}\text{Mg}$  is produced by leakage of the Ne–Na chain through  $^{23}\text{Na} (p, \gamma) ^{24}\text{Mg}$  (see Appendix A of M99). This feeds the Mg–Al chain from an external source ( $^{23}\text{Na}$ ), and leads to higher Mg–Al abundances.

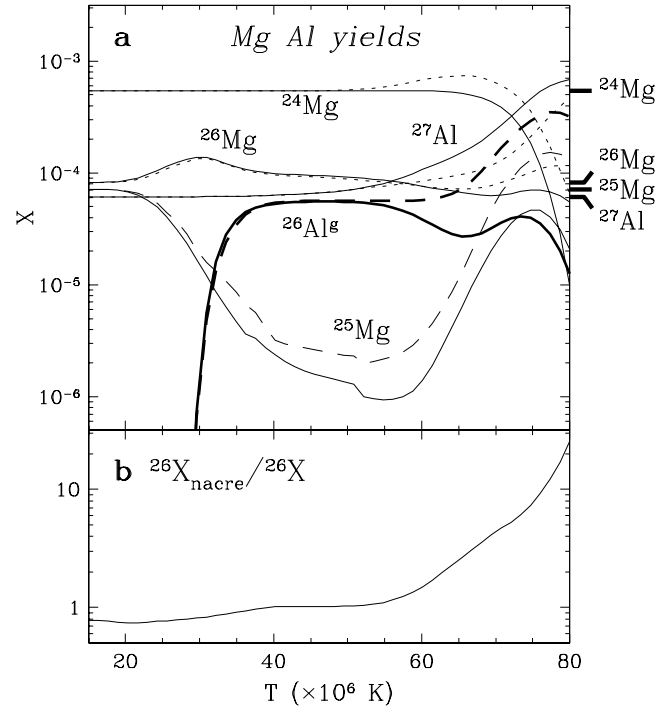


**Fig. A.2a and b.** Hydrogen burning nucleosynthesis as a function of temperature (kept constant) at which H burns. **a** Mass fractions of the stable nuclides involved in the Mg–Al chain at H exhaustion [ $X(\text{H}) = 10^{-5}$ ] versus temperature. The dotted lines represent the yields using the NACRE reaction rates (see text). The initial (solar) abundances are indicated by the horizontal thick lines at the right of the figure. **b** Ratio of  $^{26}\text{Al}$  yields predicted by the NACRE to those predicted with the old reaction rates (listed in Table A.1).

All together, the  $^{26}\text{Al}$  abundance reaches up to  $3 \times 10^{-4}$  mass fractions at  $T = 75\text{--}80 \times 10^6$  K. This is a factor of 10 to 25 higher than the abundances reached with the old reaction rates in that temperature range. This is clearly shown in Fig. A.2b which displays the ratio between the  $^{26}\text{Al}$  abundance predicted with NACRE and that predicted with the old rates as a function of H–burning temperature. The uncertainties affecting the new  $^{26}\text{Al}$  yields have been analyzed by Arnould et al. (1999). They are negligible below  $60 \times 10^6$  K and do not exceed a factor of three up to  $80 \times 10^6$  K. The consequences of those new reaction rates on the  $^{26}\text{Al}$  production in AGB model stars are presented in Sect. 4.

Let us finally note that the NACRE compilation adopts a rate for  $^{27}\text{Al} (p, \alpha) ^{24}\text{Mg}$  slower than that for  $^{27}\text{Al} (p, \gamma) ^{28}\text{Si}$  at  $T > 60 \times 10^6$  K, leading to a leakage of the Mg–Al cycle to  $^{28}\text{Si}$  at those high temperatures (cf. Arnould et al. 1999).

#### References

- Acker A., Ochsenbein F., Stenholm B., et al., 1992, Strasbourg-ESO Catalogue of Galactic Planetary Nebulae (ISBN 3-923524-41-2) 1, 1  
 Amari S., 1999, In: Bernatowicz J., Zinner E. (eds.) Astrophysical Implications of the Laboratory Study of Presolar Materials. AIP Conf. Proc. 402, p. 13

- Anders E., Grevesse N., 1989, *Geochim. Cosmochim. Acta* 53, 197
- Arnett W.D., Wefel J.P., 1978, *ApJ* 224, L139
- Arnould M., Goriely S., Jorissen A., 1999, *A&A* 437, 572
- Bernatowicz J., Zinner E., 1997, *Astrophysical Implications of the Laboratory Study of Presolar Materials*. AIP Conf. Proc. 402, 750 pp
- Boothroyd A.I., Sackmann A.-J., 1988, *ApJ* 328, 653
- Busso M., Gallino R., Waaserburg G.J., 1999, *ARA&A* 37, 239
- Champagne A.E., Cella C.H., Kouzes R.T., et al., 1988, *Nucl. Phys.* A487, 433
- Cherchneff I., Cau P., 1999, In: Le Bertre T., Lèbre A., Waelkens C. (eds.) *Asymptotic Giant Branch Stars*. IAU Symp. 191, p. 251
- Choi B.G., Wasserburg G.J., Huss G.R., 1999, *ApJ* 522, L133
- Clayton D.D., 1994, *Nat* 368, 222
- Coc A., Mochkovitch R., Oberto Y., Thibaud J.-P., Vangioni-Flam E., 1995, *A&A* 299, 479
- Dearborn D.S.P., Blake J.B., 1985, *ApJ* 288, L21
- El Eid M.F., Champagne A.E., 1995, *ApJ* 451, 298
- El Eid M.F., 1994, *A&A* 285, 915
- Forestini M., Paulus G., Arnould M., 1991, *A&A* 252, 597
- Forestini M., Charbonnel C., 1997, *A&AS* 123, 241
- Frost C.A., Cannon R.C., Lattanzio J.C., Wood P.R., Forestini M., 1998, *A&A* 332, L17
- Groenewegen M.A.T., van der Veen W.E.C.J., Matthews H.E., 1998, *A&A* 338, 491
- Guélin M., Forestini M., Valiron P., et al., 1995, *A&A* 297, 183
- Herwig F., Blöcker T., Schoenberner D., El Eid M., 1997, *A&A* 324, L81
- Hoppe P., Ott U., 1997, In: Bernatowicz J., Zinner E. (eds.) *Astrophysical Implications of the Laboratory Study of Presolar Materials*. AIP Conf. Proc. 402, p. 27
- Iliadis Ch., Schange Th., Rolfs C., et al., 1990, *Nucl. Phys.* A512, 509
- Jordi J., Hernanz M., Coc A., 1997, *ApJ* 479, L55
- Jorissen A., Smith V.V., Lambert D.L., 1992, *A&A* 261, 164
- Kahane C., Gomez-Gonzalez J., Cernicharo J., Guélin M., 1988, *A&A* 190, 167
- Kahane C., Cernicharo J., Gomez-Gonzalez J., Guélin M., 1992, *A&A* 356, 235
- Kahane C., Dufour E., Busso M., et al., 2000, *A&A* 357, 669
- Kastner J.H., Weintraub D.A., 1994, *ApJ* 434, 719
- Knödlseeder J., 1999, *ApJ* 510, 915
- Knödlseeder J., Dixon D., Bennett K., et al., 1999, *A&A* 345, 813
- Kolb U., Politano M., 1997, *A&A* 319, 909
- Langer N., Braun H., Wellstein S., 1998, In: Hillebrandt W., Müller E. (eds.) *The Proceedings of the 9th workshop on Nuclear Astrophysics*. Max-Planck-Institut für Astrophysik, p. 18
- Langer N., Heger A., Wellstein S., Herwig F., 1999, *A&A* 346, L37
- Lattimer J.M., Schramm D.N., Grossman L., 1978, *ApJ* 219, 230
- Lee T., Papanastassiou D.A., Wasserburg G.J., 1977, *ApJ* 211, L107
- MacPherson G.J., Davis A.M., Zinner E.K., 1995, *Meteoritics* 30, 365
- Mahoney W.A., Ling J.C., Wheaton W.A., Jacobson A.S., 1984, *ApJ* 286, 578
- Mauron N., Huggins P.J., 1999, *A&A* 349, 203
- Meynet G., Arnould M., Prantzos N., Paulus G., 1997, *A&A* 320, 460
- Mowlavi N., 1995, Ph. D. Thesis, Université Libre de Bruxelles<sup>11</sup>
- Mowlavi N., 1999a, *A&A* 344, 617
- Mowlavi N., 1999b, *A&A* 355, 73 (M99)
- Mowlavi N., Jorissen A., Arnould M., 1998, *A&A* 334, 153
- Naya J.E., Barthelmy S.D., Bartlett L.M., et al., 1998, *ApJ* 499, L169
- Nittler L.R., 1997, In: Bernatowicz J., Zinner E. (eds.) *Astrophysical Implications of the Laboratory Study of Presolar Materials*. AIP Conf. Proc. 402, p. 59
- Norgaard H., 1980, *ApJ* 236, 895
- Oberlack U., Bennett K., Bloemen H., 1996, *A&AS* 120, 311
- Podosek F.A., Nichols R.H. Jr., 1997, In: Bernatowicz J., Zinner E. (eds.) *Astrophysical Implications of the Laboratory Study of Presolar Materials*. AIP Conf. Proc. 402, p. 617
- Skinner C.J., Meixner M., Bobrowsky M., 1998, *MNRAS* 300, L29
- Smith V.V., Lambert D.L., 1990, *ApJS* 72, 387
- Straniero O., Gallino R., Busso M., et al., 1995, *ApJ* 440, L85
- Timmes F.X., Woosley S.E., Hartmann D.H., et al., 1995, *ApJ* 449, 204
- Timmermann R., Becker H.W., Rolfs C., Schroeder U., Trautvetter H.P., 1988, *Nucl. Phys.* A477, 105
- Van de Steene G.C., Zijlstra A.A., *Ap&SS* 108, 485
- Vangioni-Flam E., Audouze J., Chieze J.-P., 1980, *A&A* 82, 234
- Wasserburg G.J., Boothroyd A.I., Sackmann I.-J., 1995, *ApJ* 447, L37
- Winkler C., 1997, In: Winkler C., Courvoisier T., Durouchoux P. (eds.) *The Transparent Universe*. Proceedings of the 2nd INTEGRAL Workshop, ESA SP-382, p. 573
- Zinner E., 1997, In: Bernatowicz J., Zinner E. (eds.) *Astrophysical Implications of the Laboratory Study of Presolar Materials*. AIP Conf. Proc. 402, p. 5

<sup>11</sup> Available at <http://obswww.unige.ch/~mowlavi/publications>.